C.P. No. 1212

C.P. No. 1212

PROCUREMENT EXECUTIVE, MINISTRY OF DEFENCE

AERONAUTICAL RESEARCH COUNCIL

CURRENT PAPERS

Heat Transfer and Surface Pressure Measurements on Two Conical Wings in Free Flight up to $M_\infty = 4.5$

by

G. H. Greenwood

Aerodynamics Dept, R.A.E., Farnborough

LONDON: HER MAJESTY'S STATIONERY OFFICE

1972

PRICE 95*p* NET

UDC 533.693.3 : 533.692.2 : 533.6.011.6 : 533.6.048.2 : 533.6.011.5

CP No.1212*
April 1971

HEAT TRANSFER AND SURFACE PRESSURE MEASUREMENTS ON TWO CONICAL WINGS IN FREE FLIGHT UP TO $M_\infty = 4.5$

by

G. H. Greenwood

SUMMARY

Measurements in free flight at zero angle-of-attack have been made up to $M_\infty = 4.5$ of the heat transfer rates and surface pressures for two conical wings having sharp leading edges, diamond cross-sections and aspect ratios of 1.0 and 2.3 respectively. The heating rates are shown to be generally in good agreement with theoretical values using the 'intermediate enthalpy' method and the surface pressures are generally in good agreement with linearised theory. Part of these measurements were made in support of proposed RAE wind tunnel measurements of heat transfer.

---

* Replaces RAE Technical Report 71087 - ARC 33376

CONTENTS

1 INTRODUCTION

Some of the measurements presented in this Report were made in support of a proposed RAE, Bedford, wind tunnel test in which measurements are to be made at supersonic speeds of heat transfer rates and surface pressures on a delta wing. It was thought that the free-flight results would provide an interference-free standard for judging the zero angle-of-attack wind tunnel results.

The wing chosen for the wind tunnel tests is a conical delta of diamond cross-section having sharp leading edges and a planform aspect ratio of unity (see Fig.1a); two free-flight models of this shape were accordingly manufactured, one of these (model 1) having a smooth surface and the other (model 2) having a boundary-layer trip located near the leading edge. This latter was fitted in order to ensure turbulence and thus provide a common boundary-layer state for the tunnel/free-flight data comparisons.

The smooth model was tested in order to obtain information on the position of natural boundary-layer transition by studying the distribution of heat transfer rates over the wing surface. In the event, the heating rates on both the smooth and roughened model showed only very small differences between models and there existed no changes in heating levels on the individual models that could be construed as arising from a change in boundary-layer state over the surface. The effect of adding the boundary-layer trip was in fact negligible in terms of the measured heating rates and pressures.

A third model (model 3) was added to the free-flight test programme outside the scope of immediate tunnel/free-flight comparison. This model was designed to extend the measurements to a wing of the same basic form but of a larger aspect ratio.

In terms of flow conditions, the main differences between the two free-flight wing shapes are that models 1 and 2 ($\Lambda \approx 76$ degrees) have nominally subsonic leading edges for most of the test speed range (i.e. at $M_\infty < 4.13$) with leading-edge shock attachment at $M_\infty > 4.5$. Model 3 ($\Lambda = 60$ degrees) has nominally subsonic leading edges for the lower part of the speed range ($M_\infty < 2.0$) and supersonic leading edges at the higher speeds ($M_\infty > 2.0$). The leading-edge shock is attached on model 3 at $M_\infty > 2.96$. The model geometries and these various flow regimes are summarised in Table 1.

Some comparisons with theoretical pressure and heat transfer distributions are presented for both wing shapes. These comparisons relate the measured

surface pressures to values obtained from several approximate theories and the measured heat transfer rates to theoretical turbulent boundary layer values appropriate to a flat plate.

The heating rates have also been presented in terms of Stanton numbers (at Mach numbers above 2.0) to allow direct quantitative comparisons with the wind tunnel results; the method used to calculate the Stanton numbers is described in Appendix A.

Tabulations of heating rates, surface pressures and test conditions for speeds over the range M = 1.0 to 4.5 are available from Aerodynamics Department, RAE. These tabulations, presented in RAE Technical Report 71087, were prepared specifically to facilitate detailed comparisons with the proposed associated wind tunnel tests.

All the tests were conducted at an angle-of-attack nominally zero.

2 WING GEOMETRY

2.1 Model 1 (Fig.1a)

This is a conical delta wing of diamond cross-section having sharp leading edges and a planform aspect ratio of unity. The transverse leading-edge semi-angle (in a plane perpendicular to the longitudinal axis) is 15 degrees and the leading-edge sweep-back angle is approximately 76 degrees.

2.2 Model 2 (Fig.1a)

This model is geometrically identical to model 1; it differs only in that it was fitted with a boundary-layer trip (see section 3 and Fig.2).

2.3 Model 3 (Fig.1b)

This is a smooth wing (i.e. no boundary-layer trip) having the basic form of models 1 and 2 but with a leading-edge sweep-back angle of 60 degrees and a planform aspect ratio of 2.3. The transverse leading-edge semi-angle is 10 degrees.

3 BOUNDARY-LAYER TRIP

The trip consisted of a single row of approximately hemispherical steel elements spot-welded to the upper and lower surfaces of the wing at the spacing and location illustrated in Fig.2. The height of the individual tripping elements (0.5 mm) was admittedly greater than that suggested by the published literature to produce boundary-layer transition but, since the incremental wing drag due to roughness was of no consequence in the present tests, the minimum

size of element was dictated by the feasibility of manufacturing and subsequently welding the individual elements to the wing surface. Any calculations of optimum element height based on such parameters as boundary-layer thickness and critical roughness Reynolds numbers would, of course, have been relevant to only one test condition whereas the Mach and Reynolds numbers of the present test varied over a wide range.

The spacing of the individual elements was again largely dictated by engineering convenience, but in any case the published literature is far from unanimous in its recommendations in this respect. Consequently, the spacing chosen was two element diameters apart - this being also the formation favoured in much of the available literature to avoid possible twodimensional or choking effects between the elements.

One result of having over-sized tripping elements is the possibility of 'over-fixing' the boundary layer with consequent artificial thickening but, in the event, the only noticeable difference in the measurements between the smooth and roughened models that might be attributed to the boundary-layer profile as modified by the trip is the difference in surface pressure level seen over the outer region $(y/b > 0.6)$ of the semi-span in Fig.20. Elsewhere, as will be shown, the measured pressures and heating rates differed only slightly between the smooth and roughened models.

4 EXPERIMENTAL METHOD AND MODEL CONSTRUCTION

The method used to obtain aerodynamic heat transfer rates using the RAE rocket-propelled free-flight model technique is described in Refs.1 and 2. Briefly, the required test shape is constructed in the form of a thin-walled calorimeter the outer surfaces of which are wetted by the free stream and the inner surfaces of which are instrumented with thermocouples to measure the time rate of change of the in-flight wall temperature $\left(\frac{dT_w}{dt}\right)$ at selected stations. Subsequent analysis assumes a thermally thin wall. This is the so-called 'transient' method for obtaining heating rates.

The heat transfer to a given station may be described by the equation:

$$\rho_w C_{p_w} \tau_w \left(\frac{dT_w}{dt}\right) = \sum Q \qquad (4\text{-}1)$$

where ρ_w, C_{p_w} and τ_w are the density, specific heat and local thickness of the wall material and $\sum Q$ is the algebraic sum of all modes of heat transfer

at the particular station. In practice the largest constituent of $\sum Q$ is usually the convective heat transfer from the boundary layer (aerodynamic heating); the other constituents, namely transverse conductions within the wall and radiation, are usually relatively small - the conduction term being minimised by avoiding sudden discontinuities in wall thickness and avoiding heat sinks such as wall supports near the measurement stations. Radiation is calculable to some extent when the surface emissivity is known* but for most free-flight tests is negligible.

Fig.10 shows the estimated mean radiation losses from the outer and inner surfaces of the present models. Two values of surface emissivity factor have been used, one referring to polished steel ($\varepsilon = 0.14$) and one to oxidised steel ($\varepsilon = 0.79$). The true radiation losses are more likely to be nearer the curves for $\varepsilon = 0.14$ because complete oxidation of the surfaces is unlikely during the test period. Even allowing $\varepsilon = 0.79$, the radiation losses are small.

The walls of the present models were made of 0.048 in (≈ 1.2 mm) gauge mild steel sheet fabricated into the sharp-edged wing shapes by the method illustrated in Fig.3. Each thin-walled wing shell was supported against the in-flight aerodynamic loads by a large number of small-area contact pads made from a material (Syndanyo) having low thermal conductance. These pads were arranged no closer than about 1 in (25 mm) to any thermocouple station and transmitted the wing surface loads to a rigid steel internal member which was located by means of a spigot into the solid nose of the wing (see Fig.3).

Fig.4 shows the arrangement of the wings on the head ends of their respective rocket motors (to which they remained attached throughout the test) and Fig.5 shows a complete test vehicle assembly ready for launching.

After launching, the whole assembly was tracked by kinetheodolite cameras which together with radio-Doppler bearings provided the trajectory and velocity data. In-flight measurements of wall temperature, surface pressure and vehicle accelerations (see section 5) were radio-telemetered to a ground station and recorded on magnetic tape. The analogue signals so recorded were subsequently converted to digital form for processing on a high-speed computer. Ambient temperature, static pressure and wind velocity at the flight altitudes were obtained by standard RAE weapons range methods.

---

* This will usually vary with flight time as the heated wall becomes oxidised - on some models the emissivity is stabilised by pre-oxidising the wall before flight but this practice is confined to hypersonic-speed models with extremely hot walls.

5 INSTRUMENTATION

Each model was instrumented to measure surface pressures, wall temperatures and accelerations. The appropriate transducers, thermocouple cold junctions, accelerometers and the associated telemetry and radio-Doppler components were housed in an equipment bay seen in Fig.5 as the cylindrical section between the conical fairing and the rocket motor head.

5.1 Pressure measurements

5.1.1 Differential pressure (incidence measurements)

The usual method of measuring angles of incidence on RAE free-flight models is by a calibrated hemisphere-cylinder pressure probe but this was not possible in the present tests because it would have meant an unacceptable modification of the sharp wing apex. For the present tests, therefore, the wing itself was used as an incidence sensor by measuring the pressure on the upper and lower surface at stations near the apex (Figs.7 to 9). These pressure measurements were related to wing incidence angles by wind tunnel calibrations using models of the apex region having a full-scale representation of the pressure-sensing hole arrangement. In the event, the resolution of small angles of incidence was poor (see section 6.1).

5.1.2 Surface pressure

Surface pressure measurements were made on each model at the stations shown in Table 2 and Figs.7 and 9. Measurement holes of 1.3 mm diameter were drilled normal to the local surface and each was connected by a copper pipe of 1.5 mm internal diameter to one side of the diaphragm of an inductance-type pressure transducer housed in the equipment bay. The remote side of the diaphragm of each transducer was connected to a common reference-pressure chamber which was sealed at the known barometric pressure just prior to the test. Each pressure transducer thus sensed the surface pressure relative to the known reference pressure.

5.2 Wall temperature measurements

Wall temperature measurements were made on each model at the stations shown in Table 3 and Figs.6 and 8 using 0.1 mm diameter chromel/alumel wires

spot-welded to the inner surface of the wall to form 'open junction'* type thermocouples.

The cold junction for each thermocouple was located in the equipment bay encapsulated in epoxy resin against possible temperature changes in flight; the temperature of the encapsulated junctions was in any case monitored by a thermistor during flight. No measurable change in the junction temperature was noted for the present tests.

5.3 Acceleration

Accelerometers were housed in the equipment bay to sense any unwanted accelerations (i.e. lift forces) normal to the test vehicle axis. These measurements were intended primarily to monitor the general behaviour of the test vehicle rather than to allow calculations of incidence. For the present tests these accelerations were extremely small.

6 RESULTS

6.1 Incidence

The pressure-incidence calibrations resulting from the expedient of using the wings themselves as incidence sensors (5.1.1) were such that some uncertainty existed in the resolution of small angles of incidence. It was found that the differential pressure for a given angle of incidence was strongly dependent upon Mach number; any small errors in the latter resulted in relatively large errors in the derived angle of incidence.

Nevertheless, both the measured accelerations (lift forces) normal to the flight path (5.3) and the measured surface pressures and heat transfer rates, as will be seen, were everywhere consistent with a zero-incidence flight condition except perhaps at $M_\infty \geqslant 4$ for model 3 (Fig.22 and section 6.2.3). At this speed, very nearly the maximum, the rocket motor was approaching the

---

* The term 'open junction' means that the wires forming each thermocouple are welded separately to the wall and are separated by about 0.25 mm at the 'hot junction'. This method of attachment ensures the minimum mass at the junction and consequently a better response to the transient wall temperature (see Ref.3).

flame-out condition and it is not unusual at this stage of a flight for large composite test vehicles to exhibit small perturbations, induced perhaps by thermal expansions in both the rocket-motor wall and stabilising surfaces.

6.2 Surface pressures

6.2.1 Centre line chord (y/b = 0)

The surface pressure distribution along the centre line chord is presented in Figs.11 and 14 for models 2 and 3 respectively. No separate presentation is made for model 1 but comparison with the pressures from model 2 is made in Fig.12 which shows good qualitative agreement between models 1 and 2 over the chordwise region x/c = 0.2 to 0.4. Over this region, for Mach numbers of 2.0 and above, both models indicate a pressure trough which is also present, but more pronounced, in nearly the same chordal region for model 3 in Fig.14.

The pressure distribution elsewhere along the centre line chord in Fig.12 shows generally less agreement between models 1 and 2 particularly at $M_\infty > 2.0$ and the distribution for model 2 indicates a possible trough in the region of x/c = 0.8.

The distribution for model 3 seen in Fig.14 in fact shows a peak at the station x/c = 0.833 but this may well be an interference effect between sensing holes P6 and P8 (see Fig.9) which are only 13 mm apart in the stream direction.

6.2.2 Generator at y/b = 0.7

Surface pressure measurements along the y/b = 0.7 generator are shown for models 2 and 3 in Figs.15 and 18 respectively; direct comparison between models 1 and 2 is made for these pressures in Fig.16. The distributions in Fig.16 are qualitatively very similar to those of Fig.12 for the centre line chord; the most outstanding difference being in the distribution for model 1 between x/c = 0.2 and 0.4 in Fig.16, which does not show the trough apparent for model 2.

In Fig.18 the pressure distribution along the y/b = 0.7 generator for model 3 extends no further forward than the station at x/c = 0.5 owing to the lack of interior volume to accommodate pressure pipes.

6.2.3 Spanwise distributions

Figs.19 and 22 illustrate the spanwise surface pressure distributions at longitudinal station x/c = 0.833 for models 2 and 3 respectively. Comparison

of the spanwise pressures for models 1 and 2 is made in Fig.20. Fig.20 reveals close agreement in pressure level between models 1 and 2 at spanwise stations from $y/b = 0$ to about 0.6. From $y/b = 0.6$ towards the leading edge ($y/b = 1.0$) the pressure for model 1 (natural transition) is seen to be higher than that for model 2 (boundary-layer trip) for $M_\infty > 2.0$. This may be an effect arising from the boundary-layer trip on model 2 although no comparable difference in heat transfer rate was found for these models (see 6.3.3 and Fig.21).

The spanwise pressure distributions for models 1 and 2 in Fig.20 are qualitatively similar to those for model 3 in Fig.22 both showing the characteristic rise in pressure towards the leading edge. The departure from a smooth distribution at $M_\infty \geq 4.0$ for model 3 in Fig.22 may in fact be an incidence effect. In this respect it has already been pointed out (6.1) that it is not unusual for small perturbations about the zero-incidence condition to occur near the rocket-motor flame-out.

Fig.22 also shows that the heat transfer rate for this model in the outboard region ($y/b \geq 0.7$) also departs from a smooth variation at $M_\infty \geq 4.0$.

6.3 Heat transfer rates

6.3.1 Centre line chord ($y/b = 0$)

Figs.11 and 14 show the heat transfer rate along the centre line chord for models 2 and 3 respectively. As with the pressure measurements no separate presentation is made for model 1 and Fig.13 shows a comparison of the results from models 1 and 2.

The comparison in Fig.13 reveals differences in heating rate between models 1 and 2 which are small and are believed to be within the limits of the experimental uncertainties. The results for models 1 and 2 in Fig.13 and those for model 3 in Fig.14 indicate a small gradient in the heating rates along the centre line with the highest rates towards the wing apex. This gradient along the models almost certainly reflects the thickening of the boundary layer towards the trailing edge of the wings; in this respect the gradient represents an increased impedance to the kinetic heating as the boundary-layer thickness increases.

It should be noted that, because of attachment problems, the thermocouples along the centre line chord were displaced approximately 1 mm as shown in Figs.6 and 8. They were, in fact, not precisely on the wing ridge line.

6.3.2 Generator at $y/b = 0.7$

The distribution of heating rate along this generator is presented in Figs.15 and 18 for models 2 and 3 respectively. Fig.17 compares the results from models 1 and 2.

It is seen from Fig.17 that the differences in heating rate between models 1 and 2 along this generator are only slightly greater than for the centre line chord (Fig.13); nevertheless, except near $M_\infty = 4.0$, the differences are still small and are not significantly greater than the expected experimental uncertainties.

Distribution of the heating rate along the $y/b = 0.7$ generator for model 3 is presented in Fig.18. The lack of a thermocouple measuring station between $x/c = 0.7$ and 0.833 is unfortunate, inasmuch that although the plotted data can be plausibly faired over this region at Mach numbers up to 3.5, the distribution at higher Mach numbers suggests a pronounced trough in the heating rates which would appear, by tentative interpolation, to reach a minimum at about $x/c = 0.75$.

As with the pressures, the heat transfer measurements along the $y/b = 0.7$ generator on model 3 (Fig.18) extend only as far forward as $x/c = 0.5$.

6.3.3 Spanwise distributions

Spanwise distributions of heat transfer rates for models 2 and 3 are presented in Figs.19 and 22 respectively. Fig.21 presents a comparison of the results from models 1 and 2.

Like the pressure distributions across the semi-span, the heating rates exhibit a rise towards the leading edge but, unlike the pressures, there is an indication that the heating rates are at a minimum in the region of $y/b = 0.2$. This is particularly marked for model 3 (Fig.22) but is also seen for models 1 and 2 at $M_\infty \geq 3.0$ (Fig.21).

Although possible experimental uncertainties must give rise to doubts about the precise quantitative levels of the heating data there would seem to be little doubt that these minima, seen for all the models, do in fact reflect a real trend in the spanwise heating distribution.

7 COMPARISONS WITH THEORY

7.1 Surface pressure

The spanwise pressure distributions at various Mach numbers are compared with linearised theory for models 1 and 2 in Fig.23 and for model 3 in Fig.24. The Mach numbers normal to the leading edge line (M_N) are shown next to each data frame. No data for model 3 above $M_\infty = 3.5$ are presented because of suspected incidence effects at these speeds (see 6.2.3 and Fig.22).

It is seen in Figs.23 and 24 that for all the models there is generally good agreement with linear theory particularly in the wing inboard region. In Fig.23, for models 1 and 2 where $M_N < 1.0$, theoretical values of pressure coefficient were obtained for the leading-edge station ($y/b = 1.0$) from Randall's[5] modification to linear theory and it is seen that these theoretical values are consistent with a plausible extrapolation of the experimental data.

Comparison is made in Fig.25 for models 1 and 2 and in Fig.26 for model 3 with simple equivalent wedge (i.e. wedge angle = geometric slope of wing ridge) and Newtonian distributions both of which, of course, give solutions which are constant across the semi-span. It is seen that the Newtonian values always underestimate and the equivalent wedge values, in general, overestimate the measured distributions.

Also shown in Figs.25 and 26 are equivalent cone values based on the method described in Ref.6 which gives

$$\sin^{-1}\left\{\frac{a\cos\alpha + \sin\alpha}{\left(a^2 + \frac{a^2}{S_T^2} + 1\right)^{\frac{1}{2}}}\right\} \text{ (see list of symbols)}$$

for the equivalent-cone semi-angle. This results in an equivalent cone semi-angle at zero incidence ($\alpha = 0^\circ$) of 3.7 degrees for models 1 and 2 and 5.7 degrees for model 3. Theoretical surface pressures relevant to these cone semi-angles were obtained from flow tables[4].

As can be seen from Figs.25 and 26 the equivalent cone values underestimate the measured values of surface pressure but, as for the equivalent wedge and Newtonian values, better agreement with experiment is obtained at the higher free stream Mach numbers.

7.2 Heat transfer rates

The measured heating rates at three stations along the centre line chord are compared with theory for models 1 and 2 in Fig.27 and for model 3 in Fig.28. A similar comparison for a station near the leading edge on all the models is made in Fig.29.

The theoretical heating estimates at the above wing stations were based on the 'intermediate enthalpy' method (described in Ref.7) for a turbulent boundary layer on a flat plate using measured values of wall temperature and surface pressure for a given station*.

One of the aims in comparing the measured heating rates with theoretical values was to establish *a priori* the state of the boundary layer at particular wing stations and from the comparisons in Figs.27, 28 and 29 there seems no doubt that the heating rates along the centre line chord and at the leading-edge stations at $x/c = 0.833$ are consistent with a turbulent boundary layer for all the models. Elsewhere on the wing the heating rates are everywhere comparable with or greater than those at the above stations thus leaving little doubt that the heating rates represent turbulent boundary-layer values at all the measuring stations.

8 NONDIMENSIONAL HEAT TRANSFER RATES

In order to provide an unequivocal basis for comparing heat transfer rates measured for different flow characteristics and wall temperatures it is necessary to reduce these measurements to some nondimensional quantity such as Stanton number. Stanton number can be variously defined and in the present case is given as:

$$St = Q_E/\rho_\infty V_\infty (i_r - i_w) \qquad \text{(see list of symbols)}$$

and its calculation is described in Appendix A.

Distribution of the calculated Stanton numbers along the centre line chord for all the models is presented in Fig.31 and spanwise distributions in Figs.32 and 33. There is little need for comment - both the longitudinal (Fig.31) and spanwise distributions (Figs.32 and 33) are qualitatively similar to the distributions of heat transfer rate in Figs.13 and 14 and Figs.21 and 22.

---

* Wall temperatures and surface pressures were, of course, measured on different wing panels (see Fig.1) although referring to the same geometric wing station.

9 CONCLUSIONS

Measurements, up to $M_\infty = 4.5$, of surface pressures and heat transfer rates have been made at nominally zero angle-of-attack on two conical wings having diamond cross-sections with sharp leading edges and planform aspect ratios of unity and 2.3 respectively. Two models of the unit aspect ratio wing were tested - one smooth and one with a boundary layer trip located near the leading edge. The measurements led to the following conclusions:

(1) There were no differences in the measured heating rates between the smooth and boundary-layer trip model (models 1 and 2) to suggest any differences in the boundary-layer state between the two models. There were, however, small differences in the measured surface-pressure outboard of the 60 per cent semi-span station that might have been caused by the boundary-layer trip.

(2) Good agreement was generally found between the measured heat transfer rates at selected wing stations and theoretical flat plate values calculated using the 'intermediate enthalpy' method for a turbulent boundary layer (Figs.27, 28 and 29). This agreement, together with the general level of heating at the other stations, suggests that the boundary layer over most of the wing surface was, on all models, non-laminar and probably fully turbulent.

(3) Comparison of the surface-pressure measurements with linear theory showed that agreement was good for the aspect ratio unity wings (models 1 and 2, Fig.23) particularly at the higher speeds ($M_\infty > 2$) and in the inboard region of the wings. A similar comparison for the aspect ratio 2.3 wing (model 3, Fig.24) showed good agreement up to $M_\infty = 3.5$, again particularly in the inboard region. Nearer the leading edge on this model there were differences in detail between experiment and theory but the general level in surface pressure (at $M_\infty = 3.0$ and 3.5 at least) was in good agreement with the theoretical level. No comparisons for the aspect ratio 2.3 wing were made above $M_\infty = 3.5$ because of suspected incidence effects.

(4) Comparisons between the measured surface pressures for all the models with the approximate equivalent cone, equivalent wedge and Newtonian solutions (Figs.25 and 26) showed poor agreement even at the highest test Mach number of 4.5 where agreement was best.

Appendix A

CALCULATION OF STANTON NUMBERS

The nondimensional local Stanton numbers, St, are defined for the present tests as

$$St = \frac{Q_E}{\rho_\infty V_\infty (i_r - i_w)} \tag{A-1}$$

where Q_E, ρ_∞ and V_∞ are obtained directly from the experimental measurements and the enthalpy term i_w is related graphically with the measured wall temperature, T_w, through Fig.30.

The recovery enthalpy, i_r, is related to the enthalpy and Mach number of the flow just outside the boundary layer (suffixed e) by

$$i_r = i_e \left[1 + r M_e^2 \frac{\gamma - 1}{2} \right] \tag{A-2}$$

where r is the enthalpy recovery factor assumed to have the empirical value of 0.89 for a turbulent* boundary layer.

In the calculation of i_e and M_e it is assumed that the flow just outside the boundary layer is related to free stream conditions by the perfect-gas oblique-shock equations as presented, for example, in Ref.4. These equations permit the Mach number and temperature (and hence enthalpy) of the flow just outside the boundary layer to be determined in terms of the measured pressure ratio, p_s/p_∞, on the wing surface; it being assumed that the measured surface pressure, p_s, is unchanged through the boundary layer and that $p_s = p_e$.

The pressure ratio p_e/p_∞ $(= p_s/p_\infty)$ is related to the oblique-shock wave angle, θ, by

$$\frac{p_e}{p_\infty} = \frac{2\gamma M_\infty^2 \sin^2 \theta - (\gamma - 1)}{(\gamma + 1)} \tag{A-3}$$

and the density ratio by

$$\frac{\rho_e}{\rho_\infty} = \frac{(\gamma + 1) M_\infty^2 \sin^2 \theta}{(\gamma - 1) M_\infty^2 \sin^2 \theta + 2} \tag{A-4}$$

---

* The assumption of a turbulent boundary layer for the present tests arises from the comparisons of the measured and theoretical heat transfer rates in Figs.27 to 29.

and, since the static temperature ratio across the oblique shock is given by

$$\frac{T_e}{T_\infty} = \frac{[2\gamma M_\infty^2 \sin^2\theta - (\gamma - 1)][(\gamma - 1)M_\infty^2 \sin^2\theta + 2]}{(\gamma + 1)^2 M_\infty^2 \sin^2\theta}$$

it follows from equations (A-3) and (A-4) that

$$\frac{T_e}{T_\infty} = \frac{p_e}{p_\infty}\frac{\rho_\infty}{\rho_e} . \tag{A-5}$$

Further, the density ratio is related to the pressure ratio, with $\gamma = 1.4$, by

$$\frac{\rho_e}{\rho_\infty} = \frac{6\frac{p_e}{p_\infty} + 1}{\frac{p_e}{p_\infty} + 6} . \tag{A-6}$$

Hence, by combining equations (A-5) and (A-6), T_e/T_∞ is given directly in terms of the pressure ratio by

$$\frac{T_e}{T_\infty} = \frac{\frac{p_e}{p_\infty}\left(\frac{p_e}{p_\infty} + 6\right)}{6\frac{p_e}{p_\infty} + 1} \tag{A-7}$$

with no assumptions regarding the magnitude of the flow deflection angle or shock wave angle.

The Mach number just outside the boundary layer, M_e, is related to the pressure ratio by

$$M_e^2 = \frac{M_\infty^2\left[(\gamma + 1)\frac{p_e}{p_\infty} + (\gamma - 1)\right] - 2\left[\left(\frac{p_e}{p_\infty}\right)^2 - 1\right]}{\frac{p_e}{p_\infty}\left[(\gamma - 1)\frac{p_e}{p_\infty} + (\gamma + 1)\right]}$$

which for $\gamma = 1.4$ reduces to

$$M_e^2 = \frac{M_\infty^2\left[6\frac{p_e}{p_\infty} + 1\right] - 5\left[\left(\frac{p_e}{p_\infty}\right)^2 - 1\right]}{\frac{p_e}{p_\infty}\left(\frac{p_e}{p_\infty} + 6\right)} \tag{A-8}$$

M_e is thus obtained in terms of the free stream Mach number, M_∞, and of the pressure ratio with again no assumptions regarding the magnitude of the flow deflection angle or shock-wave angle.

Evaluation of i_r from equation (A-2) may now follow, with T_e obtained from equation (A-7)

$$T_e = T_\infty \left[\frac{\frac{p_e}{p_\infty}\left(\frac{p_e}{p_\infty} + 6\right)}{6\frac{p_e}{p_\infty} + 1} \right]$$

and, i_e from the enthalpy-temperature relationship in Fig.30.

Table 1

SUMMARY OF TESTS

Model	Geometry						Test conditions				
	Λ^o	δ^o	β^o	AR	C mm	Max. M_∞	Max. R_E	Nominal α^o	LEs nominally sonic at M_∞ =	LE shock attached at M_∞ =	Boundary-layer trip fitted
1	75.96	15	15.4	1.0	914.4	4.5	90×10^6	0	4.13	> 4.5	No
2	75.96	15	15.4	1.0	914.4	4.5	88×10^6	0	4.13	> 4.5	Yes
3	60.0	10	11.58	2.3	395.9	4.5	40×10^6	0	2.0	> 2.96	No

Λ^o = leading-edge sweep-back angle

δ^o = leading-edge semi-angle measured normal to centre line chord

β^o = leading-edge semi-angle measured normal to leading edge

AR = aspect ratio

C = wing centre line chord

M_∞ = free stream Mach number

R_E = free stream Reynolds number, based on centre line chord, approx. linear with M_∞

α^o = angle of pitch incidence

Table 2

LOCATION OF PRESSURE HOLES

(see also Figs.7 and 9)

Pressure hole	Models 1 and 2		Model 3	
	x/c	y/b	x/c	y/b
1	0.2	0*	0.3	0*
2	0.3	0*	0.4	0*
3	0.4	0*	0.5	0*
4	0.5	0*	0.6	0*
5	0.6	0*	0.7	0*
6	0.7	0*	0.8	0*
7	0.8	0*	0.9	0*
8	0.9	0*	0.833	0*
9	0.833	0*	0.833	0.1
10	0.833	0.1	0.833	0.2
11	0.833	0.2	0.833	0.3
12	0.833	0.3	0.833	0.4
13	0.833	0.4	0.833	0.5
14	0.833	0.5	0.833	0.6
15	0.833	0.6	0.833	0.7
16	0.833	0.7	0.833	0.8
17	0.833	0.8	0.3	0.5
18	0.833	0.9	0.4	0.6
19	0.2	0.7	0.5	0.7
20	0.3	0.7	0.6	0.7
21	0.4	0.7	0.7	0.7
22	0.5	0.7	0.8	0.7
23	0.6	0.7	0.9	0.7
24	0.7	0.7	-	-
25	0.8	0.7	-	-
26	0.9	0.7	-	-

* y/b = 0 is a nominal station.
Pressure holes were displaced by approximately 0.6 mm (see Figs.7 and 9).

Table 3

LOCATION OF THERMOCOUPLES

(see also Figs.6 and 8)

Thermocouple	Models 1 and 2		Model 3	
	x/c	y/b	x/c	y/b
F1	0.2	0*	0.3	0*
F2	0.3	0*	0.4	0*
F3	0.4	0*	0.5	0*
F4	0.5	0*	0.6	0*
F5	0.6	0*	0.7	0*
F6	0.7	0*	0.8	0*
F7	0.8	0*	0.9	0*
F8	0.9	0*	0.833	0*
F9	0.833	0*	0.833	0.1
F10	0.833	0.1	0.833	0.2
F11	0.833	0.2	0.833	0.3
F12	0.833	0.3	0.833	0.4
F13	0.833	0.4	0.833	0.5
F14	0.833	0.5	0.833	0.6
F15	0.833	0.6	0.833	0.7
F16	0.833	0.7	0.833	0.8
F17	0.833	0.8	0.3	0.5
F18	0.833	0.9	0.4	0.6
F19	0.2	0.7	0.5	0.7
F20	0.3	0.7	0.6	0.7
F21	0.4	0.7	0.7	0.7
F22	0.5	0.7	0.9	0.7
F23	0.6	0.7	-	-
F24	0.7	0.7	-	-
F25	0.8	0.7	-	-
F26	0.9	0.7	-	-

* y/b = 0 is a nominal station.
Thermocouples were displaced approximately 1 mm (see Figs.6 and 8).

SYMBOLS

a	tangent of surface angle at the wing centre line (d/2c, Fig.1)
b	local semi-span of wing
c	centre line chord
C_p	pressure coefficient = $(p - p_\infty)/q_\infty$
C_{p_w}	specific heat of the wall material (equation (4-1))
d	diameter of boundary-layer trip element (Fig.2)
d	thickness of wing at its base (Fig.1)
F	denotes a thermocouple station
i	enthalpy of air
M	Mach number
p	static pressure
p_s	static pressure on the wing surface
P	denotes a pressure station
q	free stream kinetic pressure
Q	heat transfer rate
r	enthalpy recovery factor
St	Stanton number
S_T	tangent of planform semi-angle = tan $(90^\circ - \Lambda^\circ)$
t	time
T	temperature
V	flow velocity
x	chordwise distance from wing apex
y	spanwise distance from wing centre line
α	angle of incidence
γ	specific heat ratio for air
ϵ	emissivity of wing surface
θ	shock-wave angle
Λ	angle of leading edge sweepback
ρ	density
ρ_w	density of wall material (equation (4-1))
τ_w	local thickness of the wall (equation (4-1))

SYMBOLS (Contd)

Subscripts

e	conditions just outside boundary layer
E	experimental quantity
N	normal to leading edge
r	recovery conditions
s	on the wing surface
w	conditions at the wall
∞	free stream conditions

REFERENCES

No.	Author(s)	Title, etc.
1	J. Picken D. Walker	Techniques for the investigation of aerodynamic heating effects in free flight. AGARD Report 376 (1961) ARC 23125 (1961)
2	J. Picken	Notes on a reduction procedure for temperature data from free-flight telemetry. ARC 21389 (1959)
3	F.H. Irvine J. Picken G.H. Greenwood	Measurements of the response of various thermo-couple arrangements. ARC 26187 (1964)
4	Ames Research Staff	Equations, tables, and charts for compressible flow. NACA Report 1135 (1953)
5	D.G. Randall	A technique for improving the predictions of linearised theory on the drag of straight-edge wings. ARC CP 394 (1957)
6	L.C. Squire	Pressure distributions and flow patterns on some conical shapes with sharp edges and symmetrical cross-sections at M = 4.0. ARC R & M 3340 (1962)
7	L.F. Crabtree R.L. Dommett J.G. Woodley	Estimation of heat transfer to flat plates, cones and blunt bodies. ARC 27233 (1965)

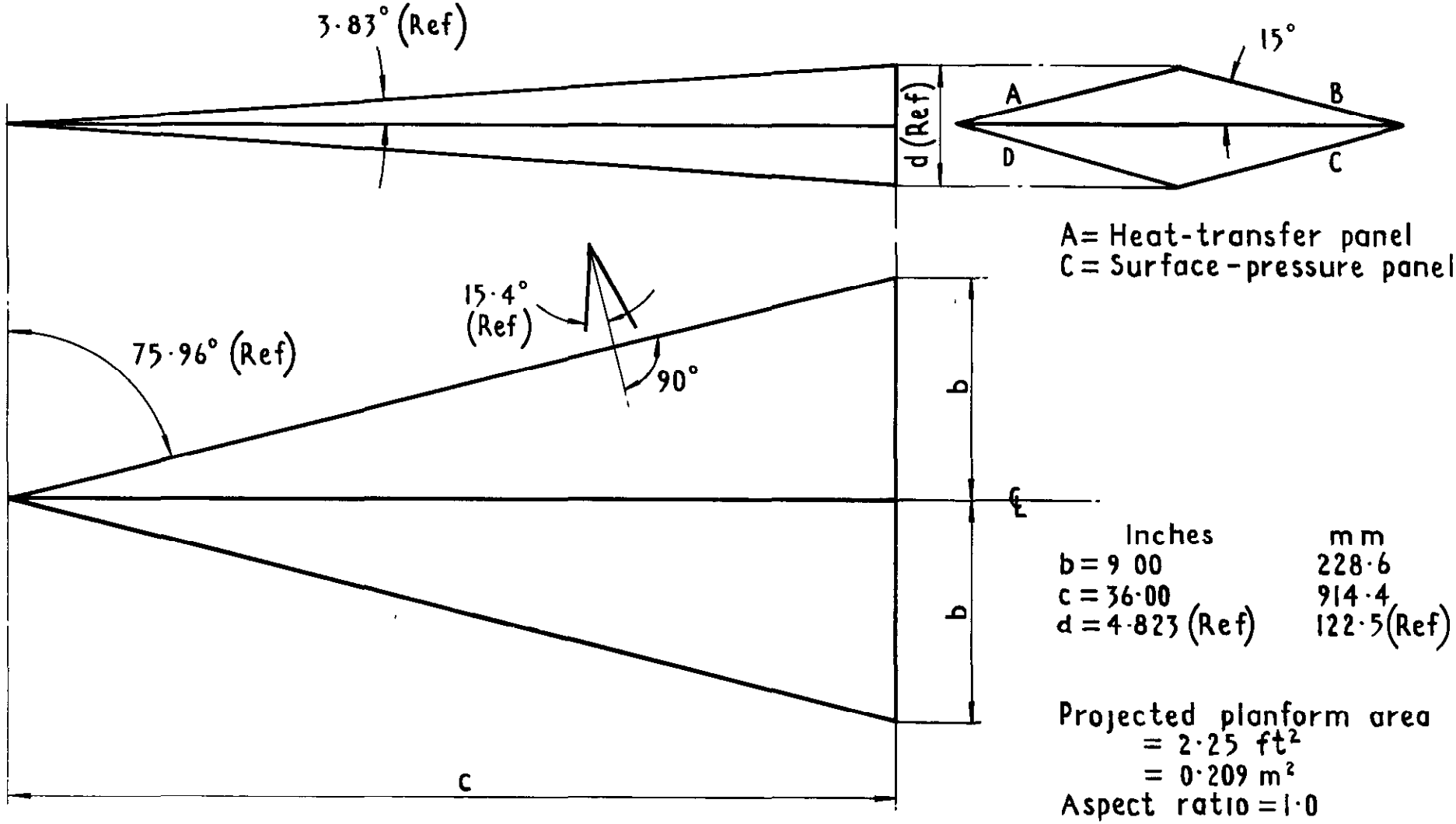

a Models 1 & 2 (model 2 had boundary-layer trip, see Fig.2)

Fig 1a Model geometry

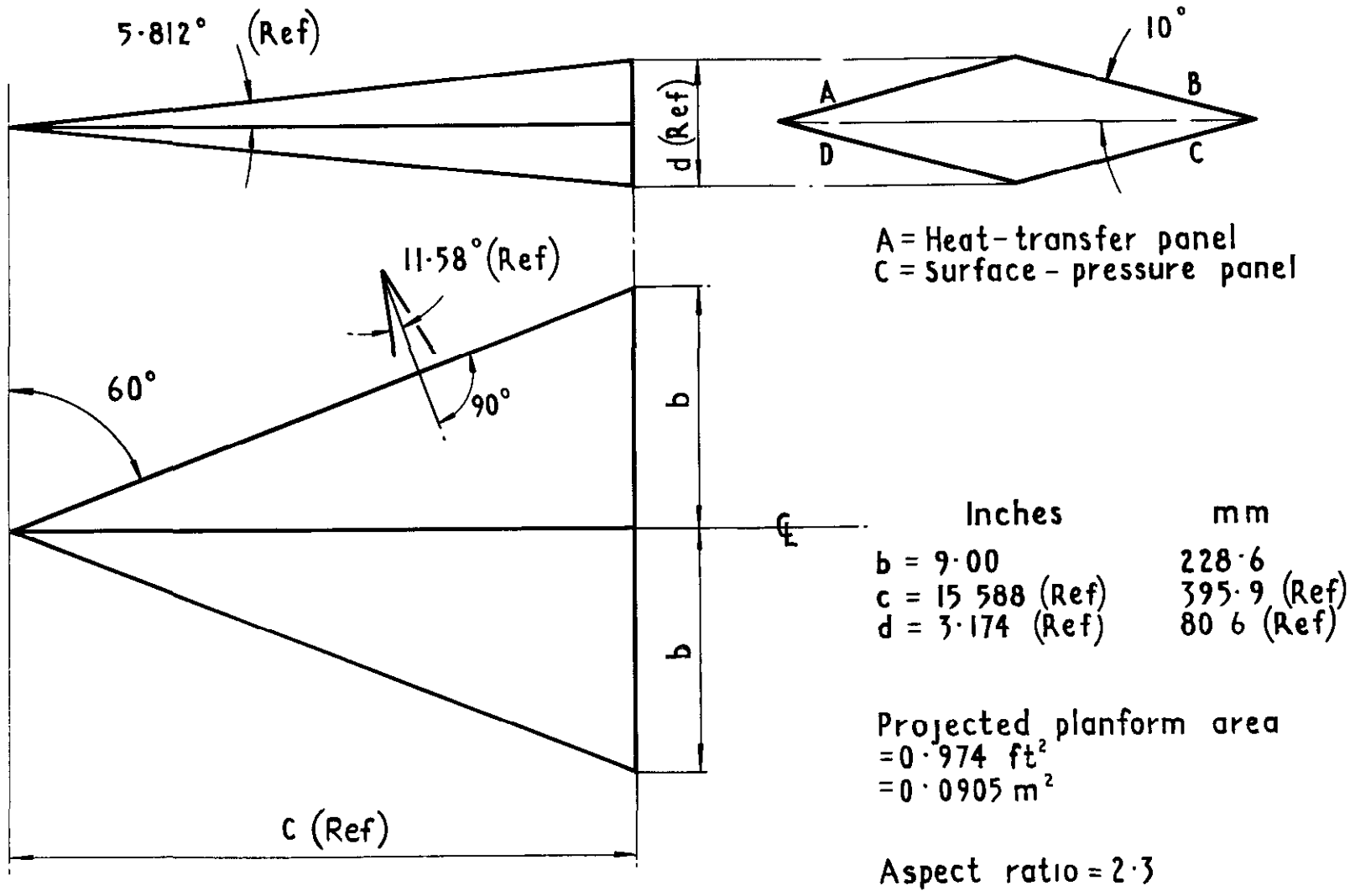

b Model 3

Fig.1b Model geometry

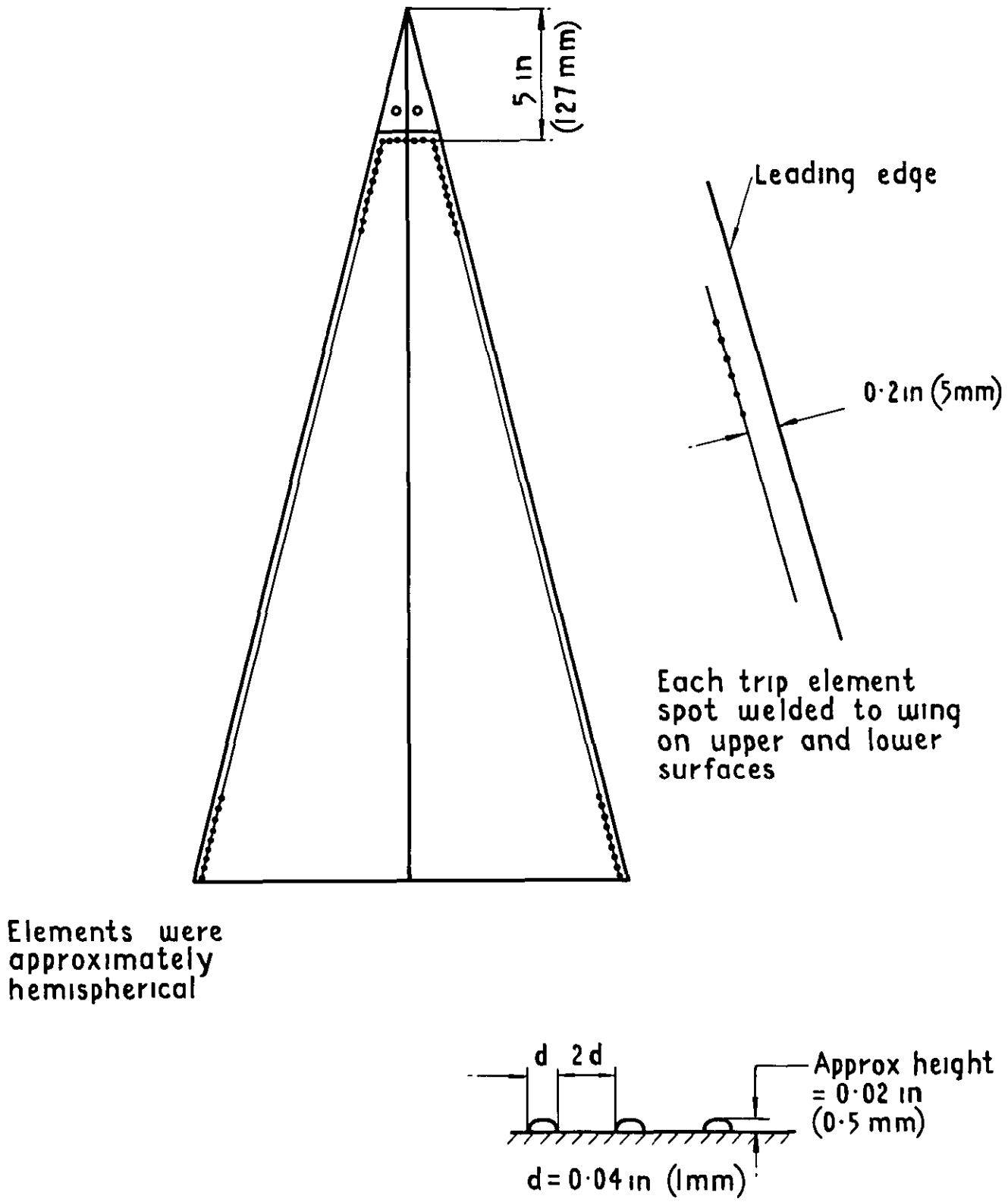

Fig.2 Details of boundary-layer trip on model 2

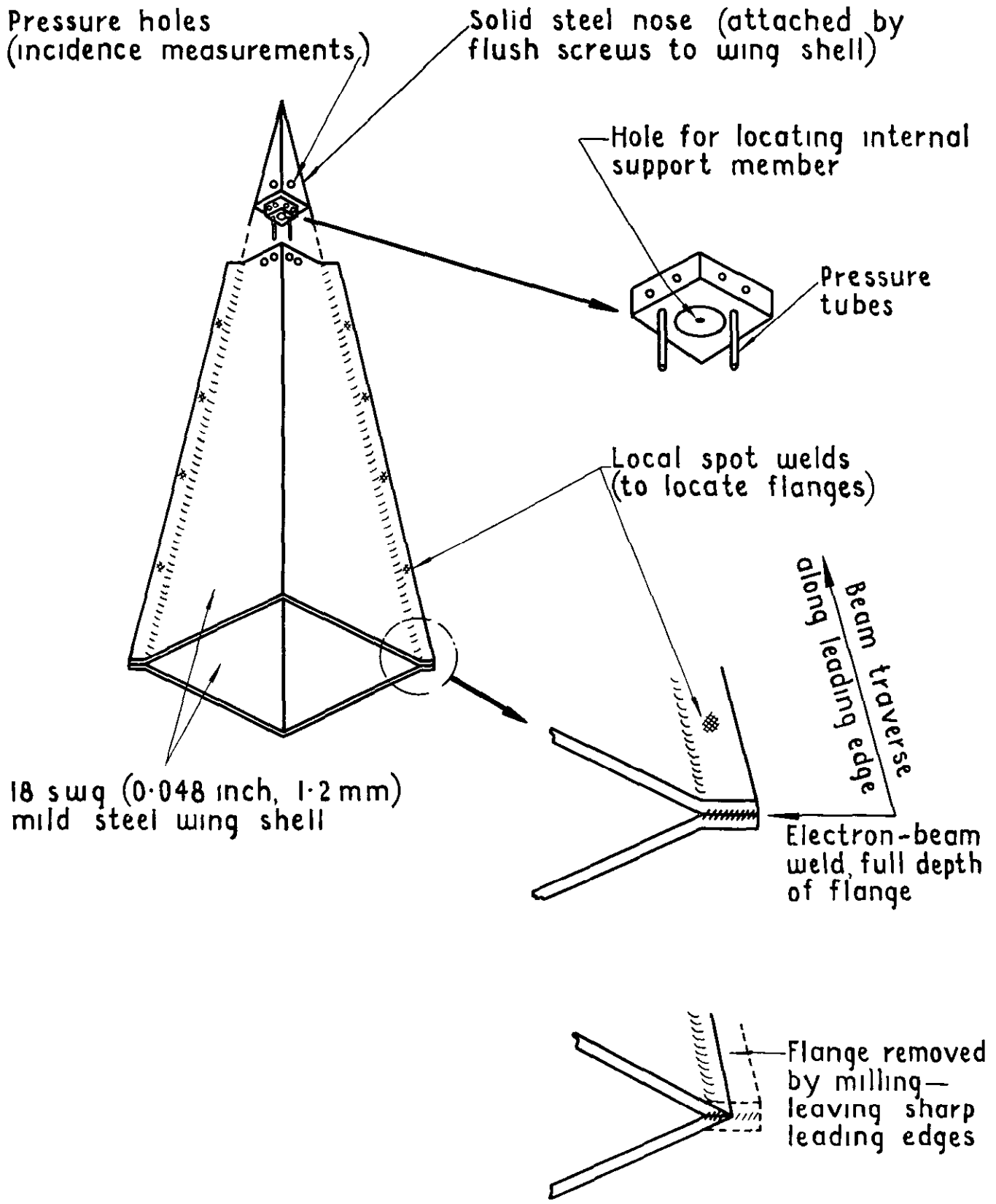

Fig 3 Construction of sharp leading edges
— all models

Model.1.

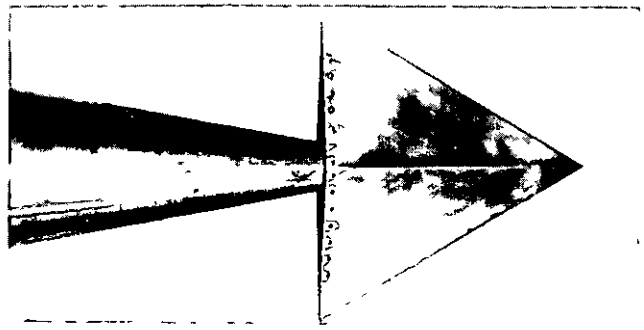

Model.3.

Fig.4.

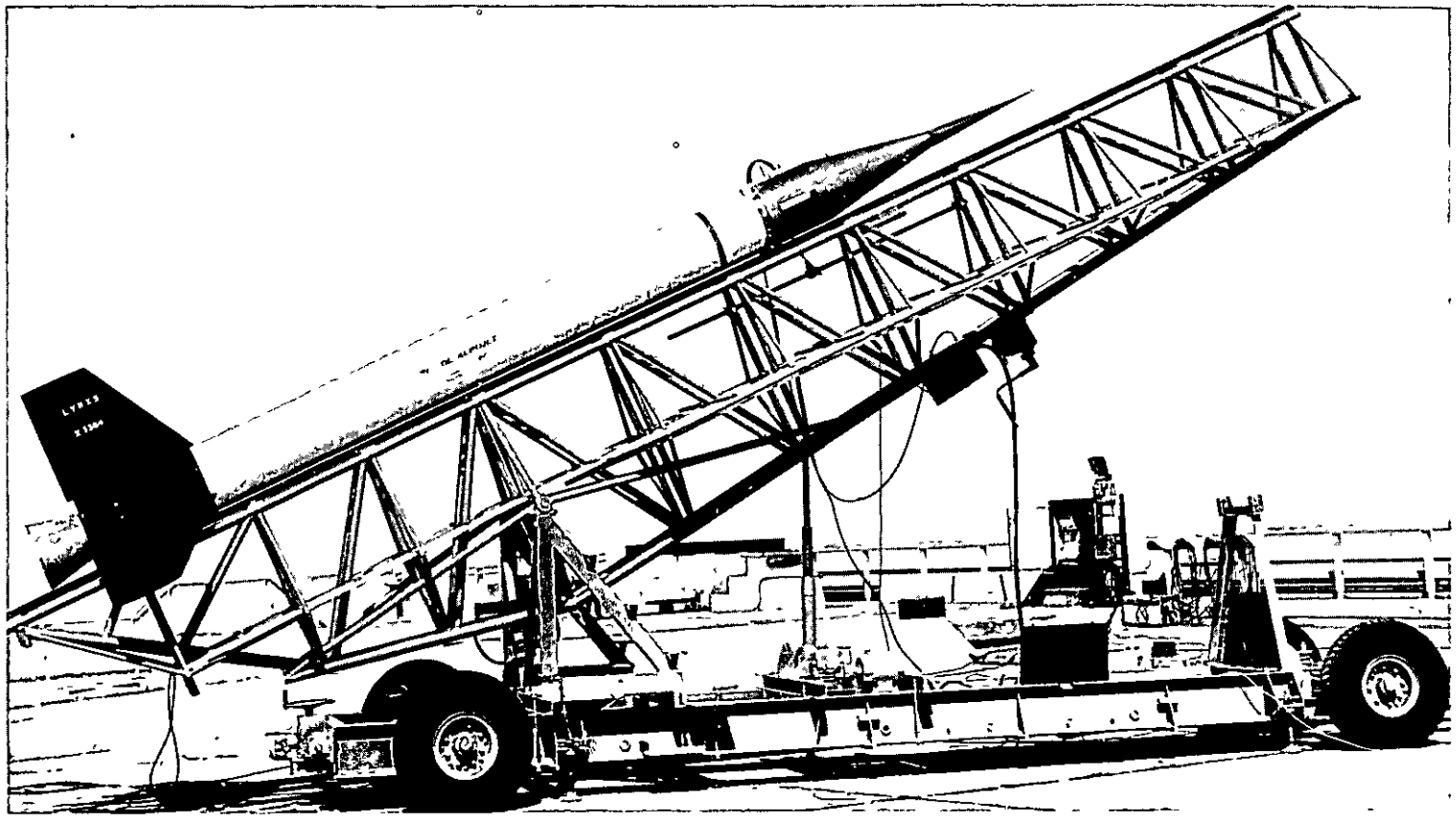

Fig.5. Test vehicle on launcher.

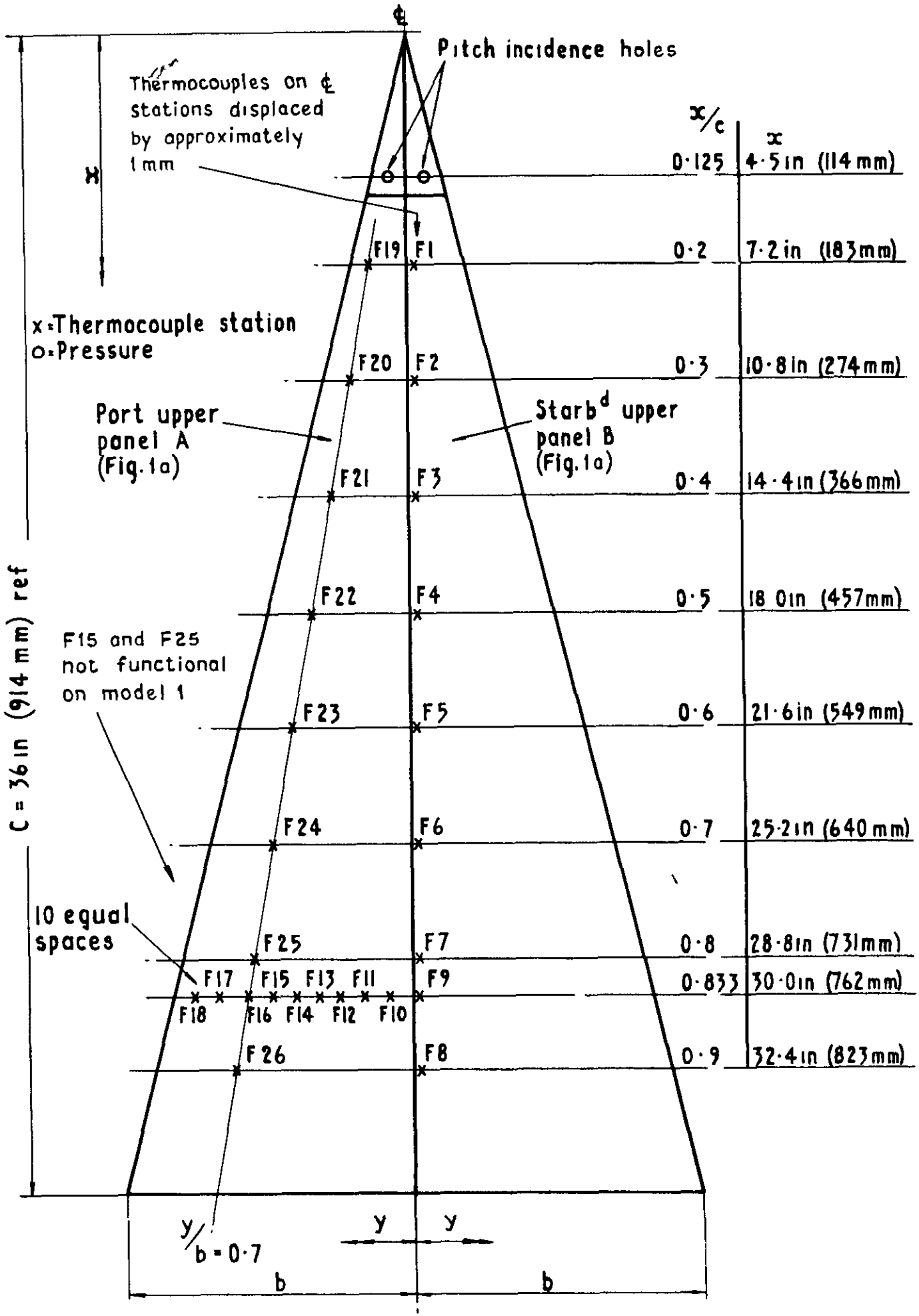

Fig.6 Measurement stations – upper surfaces – models 1 & 2

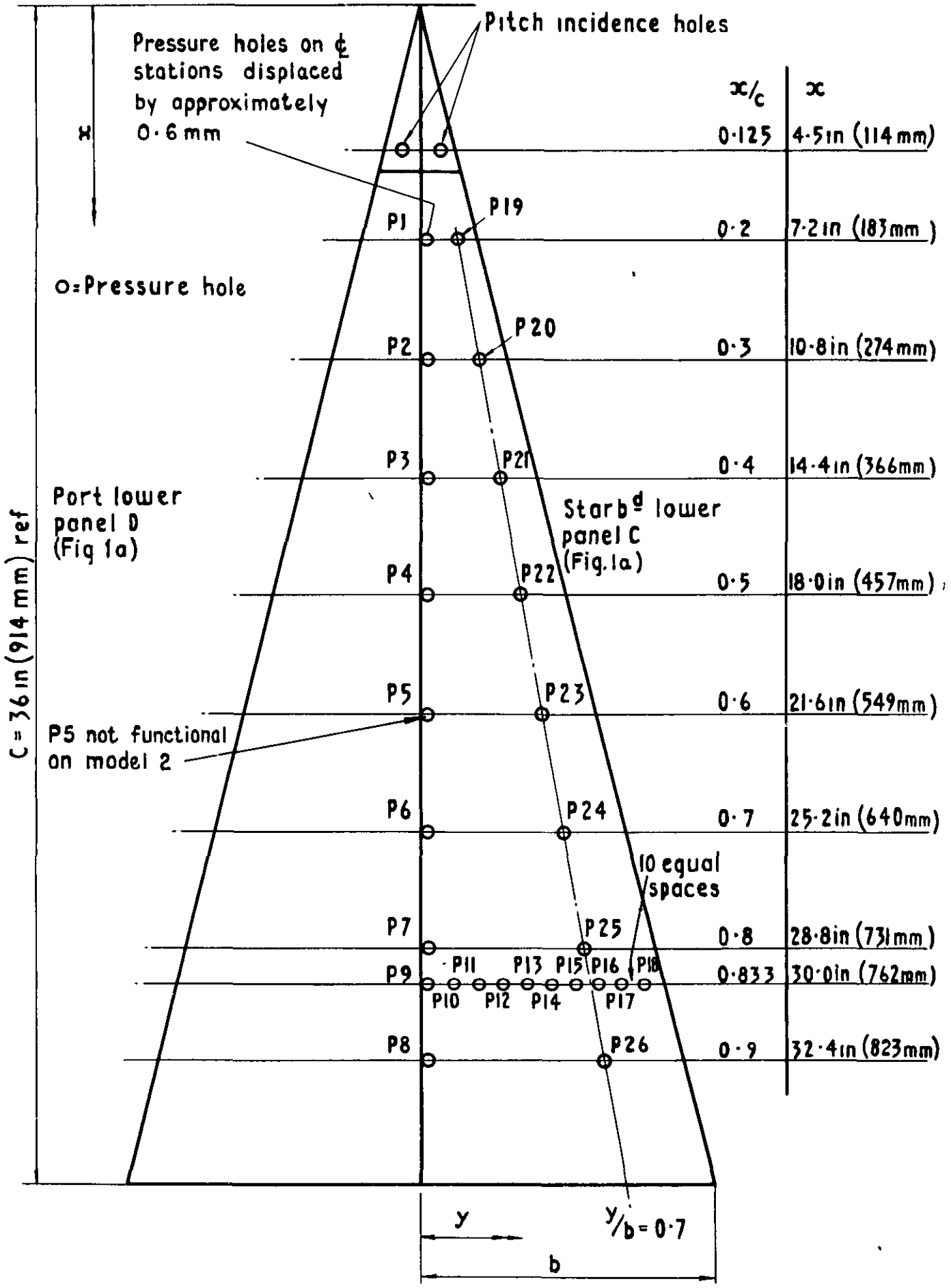

Fig.7 Measurement stations - lower surfaces - models 1 & 2

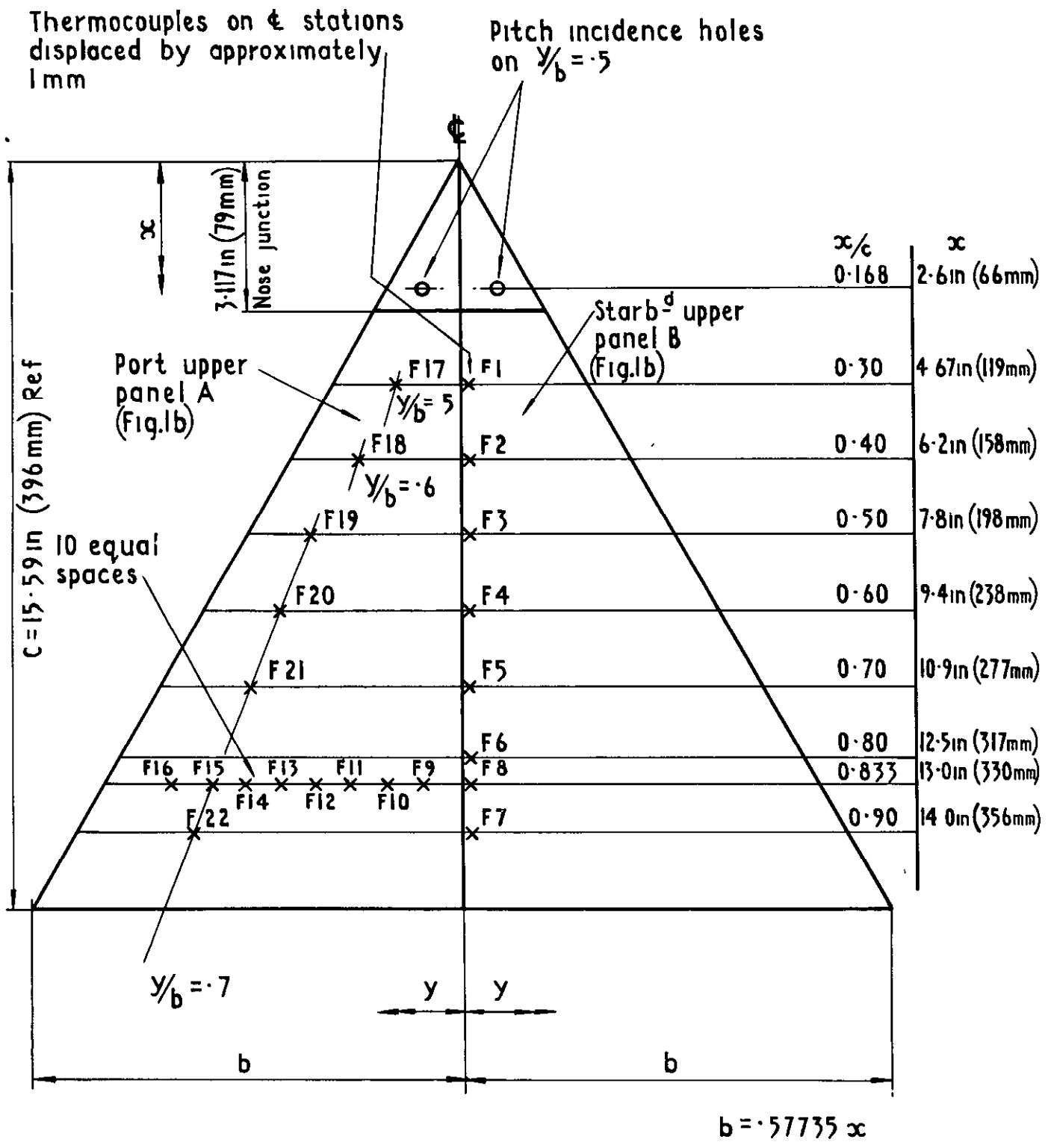

Fig.8 Measurement stations – upper surfaces – model 3

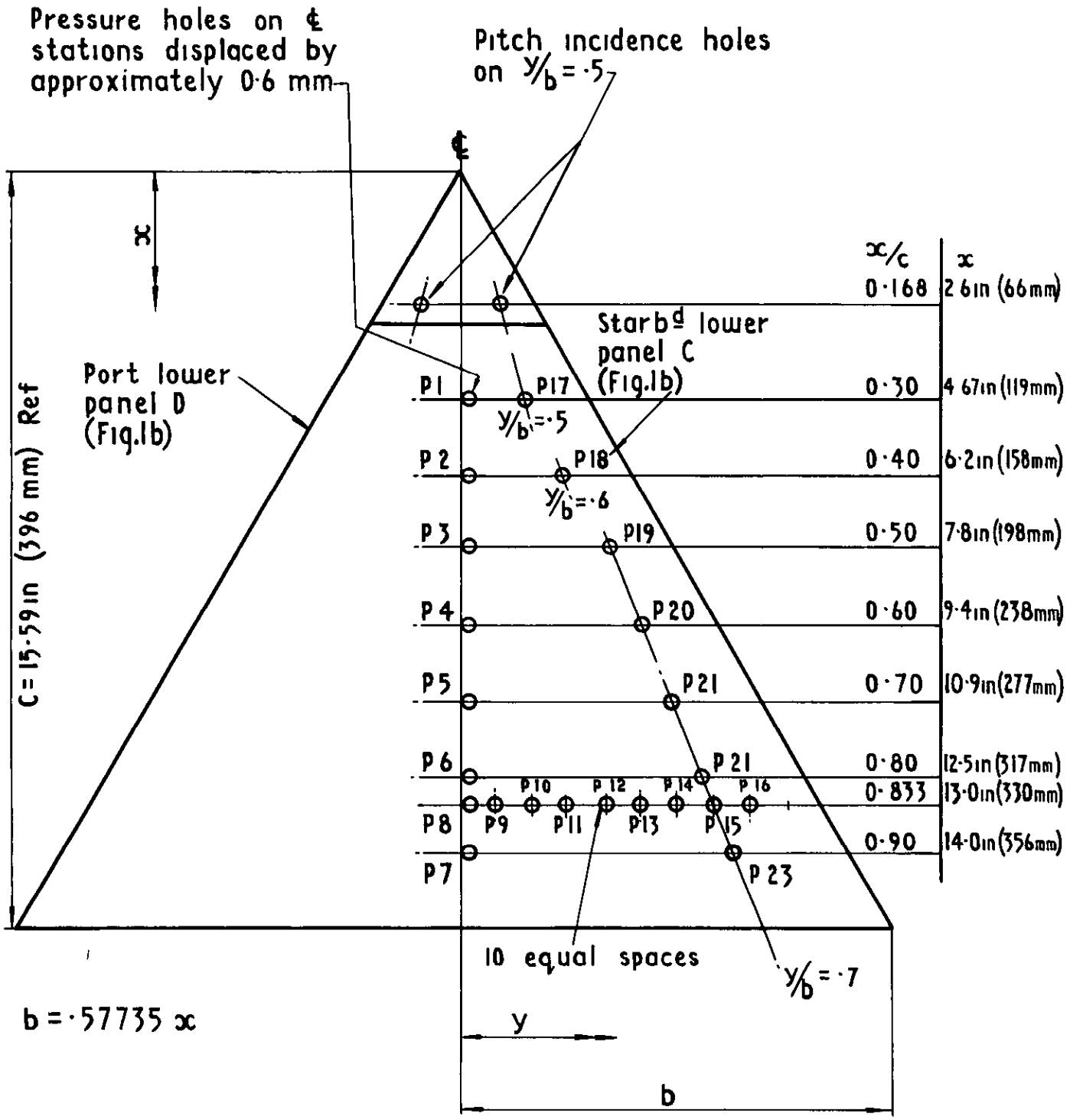

o = Pressure hole

Fig 9 Measurement stations - lower surfaces - model 3

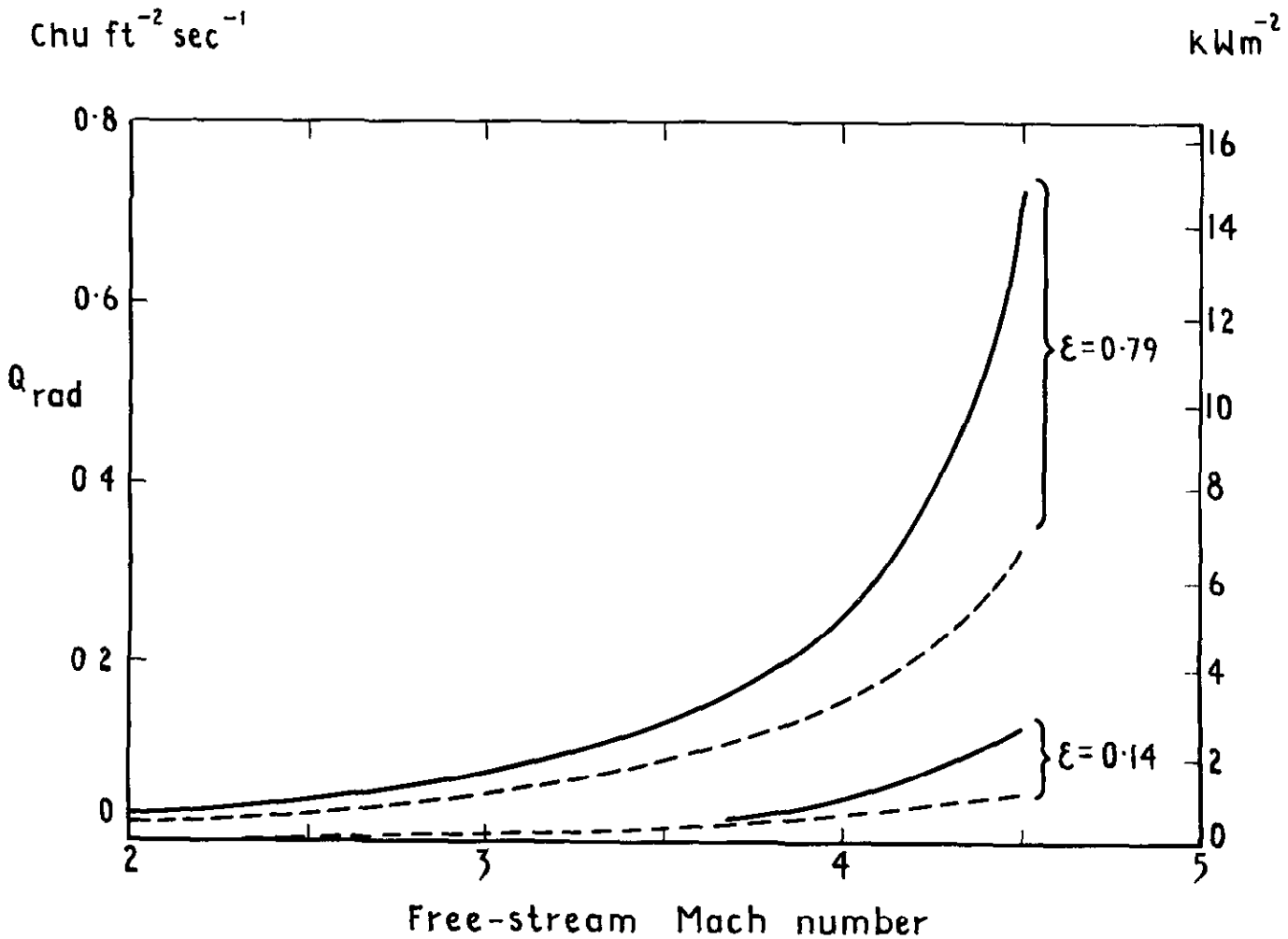

– – – – Models 1 and 2
——— Model 3

$Q_{rad} = \beta \varepsilon T_w^4$

β = Stefan – Boltzmann constant = $2{\cdot}78 \times 10^{-12}$ Chu ft^{-2} sec^{-1} (°k)$^{-4}$
= $56{\cdot}75 \times 10^{-12}$ kWm^{-2} (°k)$^{-4}$

ε = Surface emissivity factor = 0·14 (polished steel)
= 0·79 (oxidised steel) } Ref 7

Fig.10 Estimated mean radiative heat losses, $Q_{rad.}$, from outer and inner wing surfaces

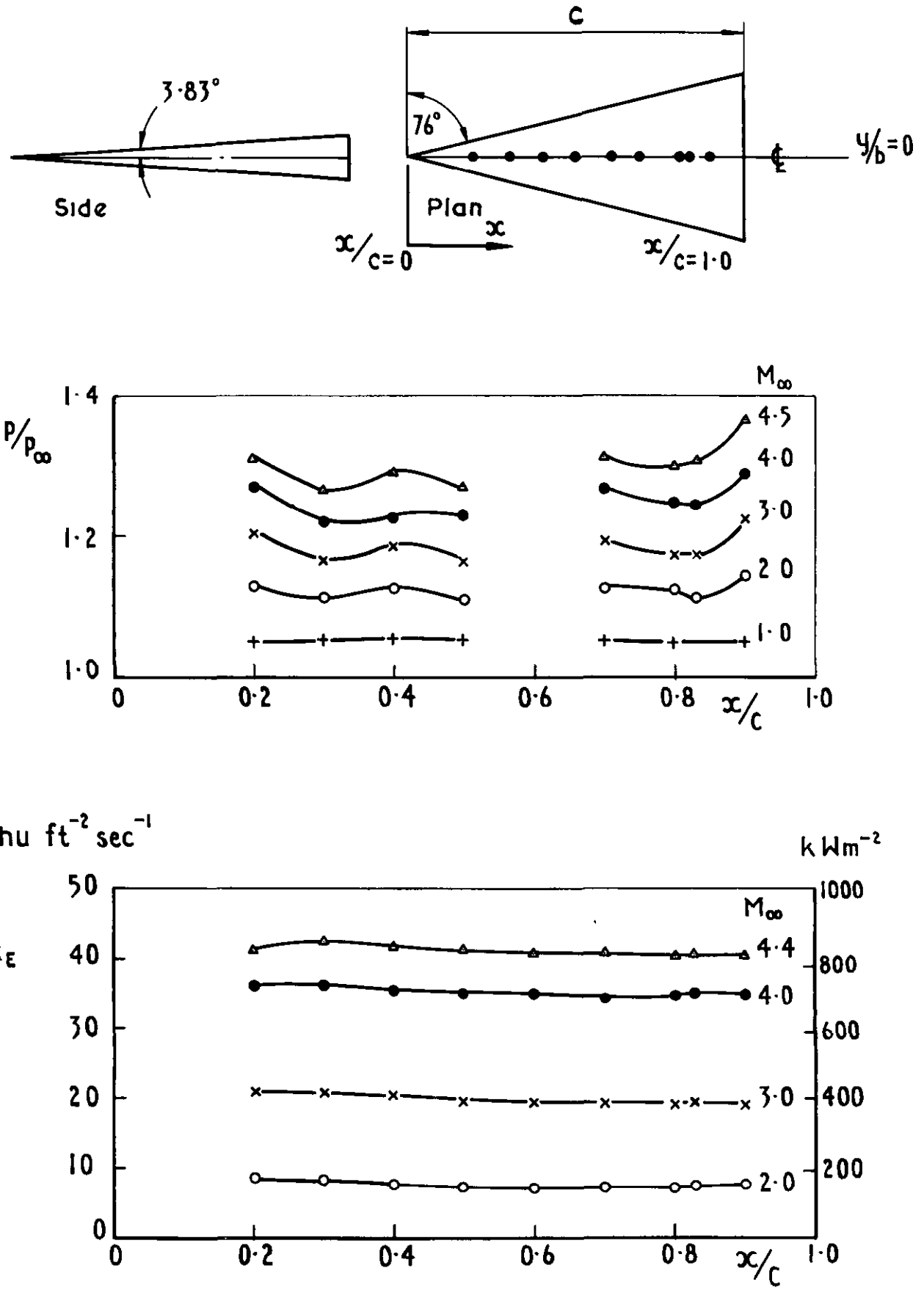

Fig 11 Distribution of pressure and heat-transfer rate along centre-line chord, $y/b=0$ – model 2 (BL trip)

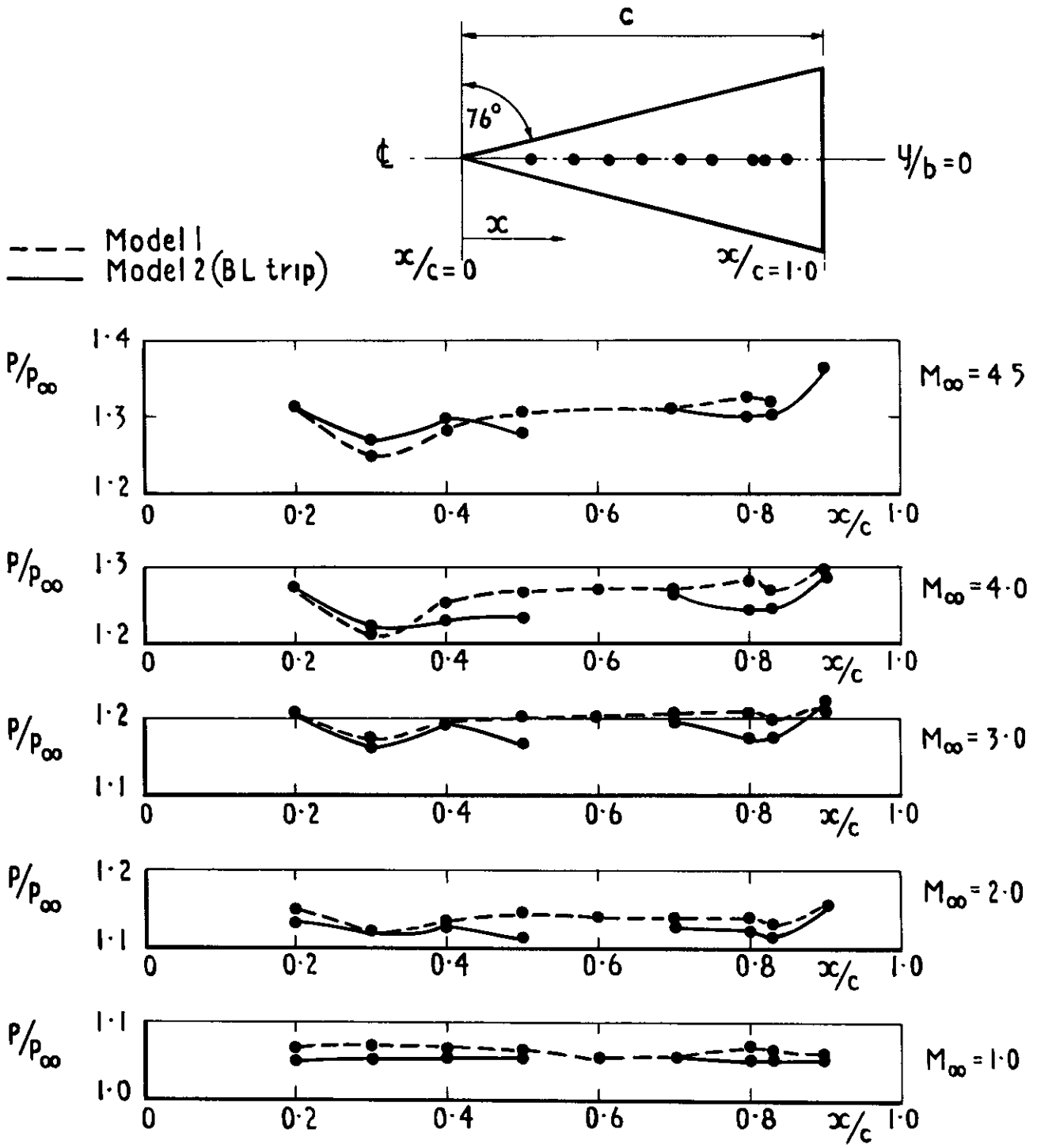

Fig 12 Comparison of pressure distribution along centre-line chord, $y/b = 0$ – models 1 & 2

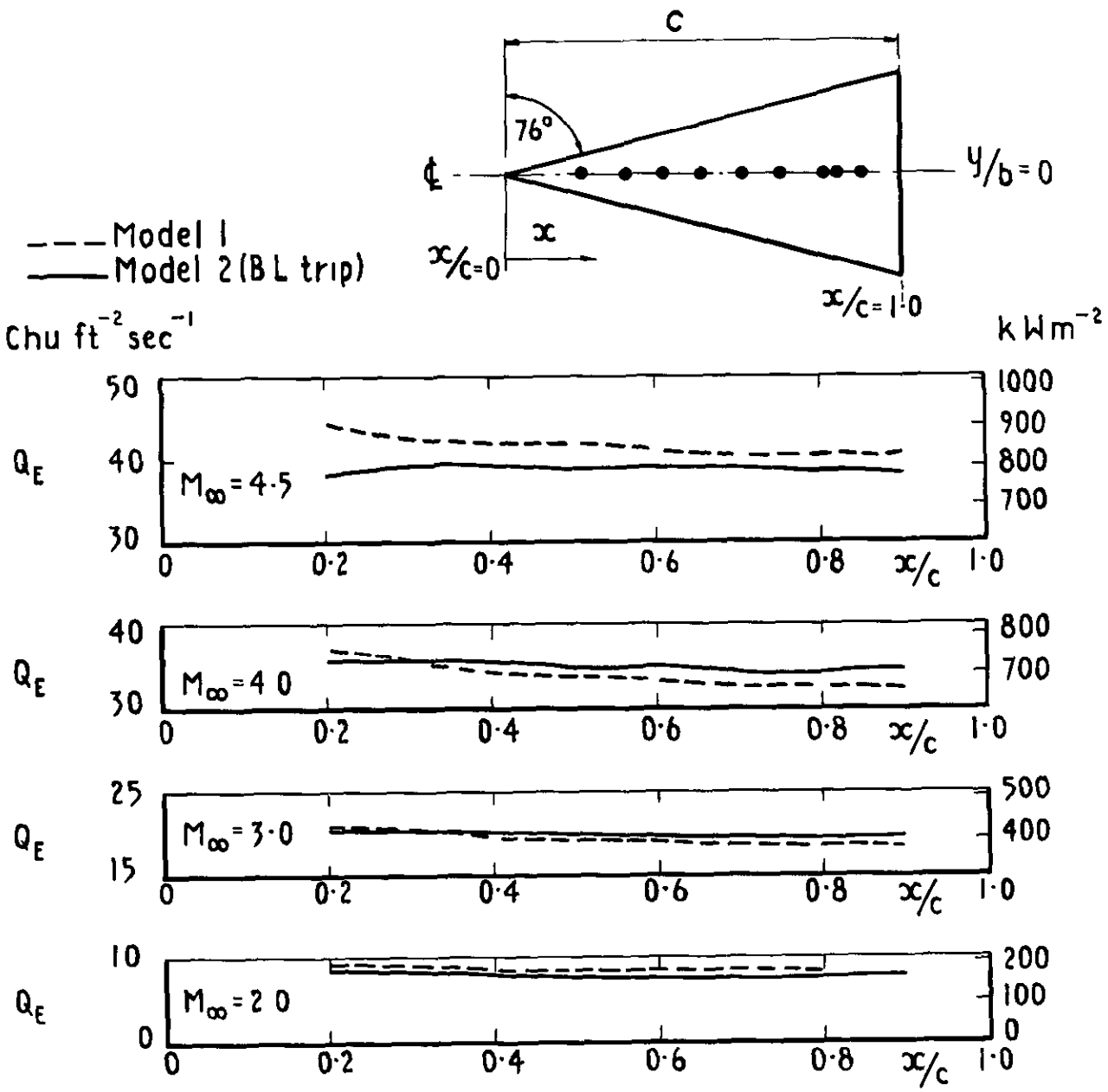

Fig 13 Comparison of heat-transfer rate along centre-line chord, $y/_b = 0$ – models 1 & 2

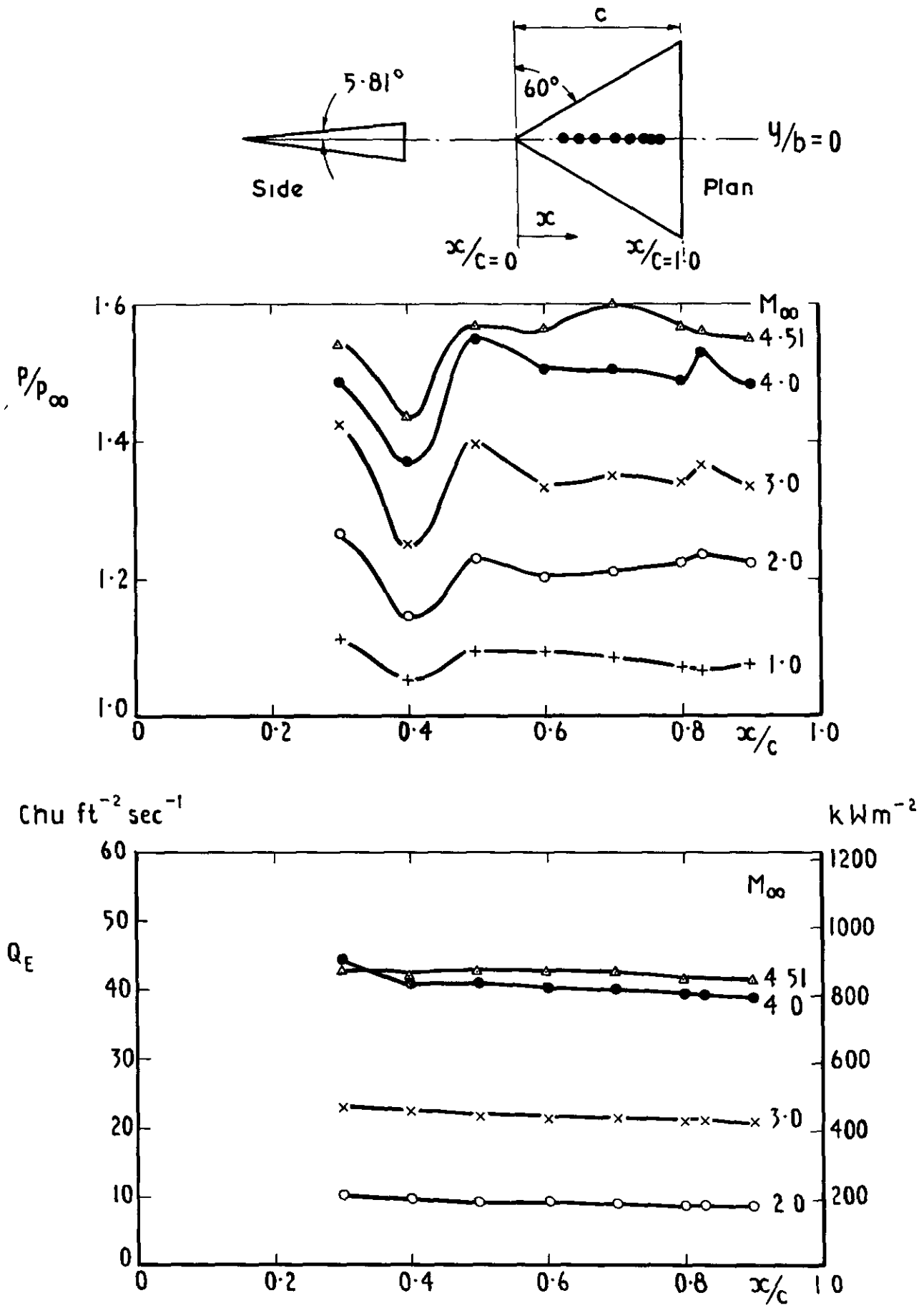

Fig 14 Distribution of pressure and heat-transfer rate along centre-line chord, $y/b = 0$ – model 3

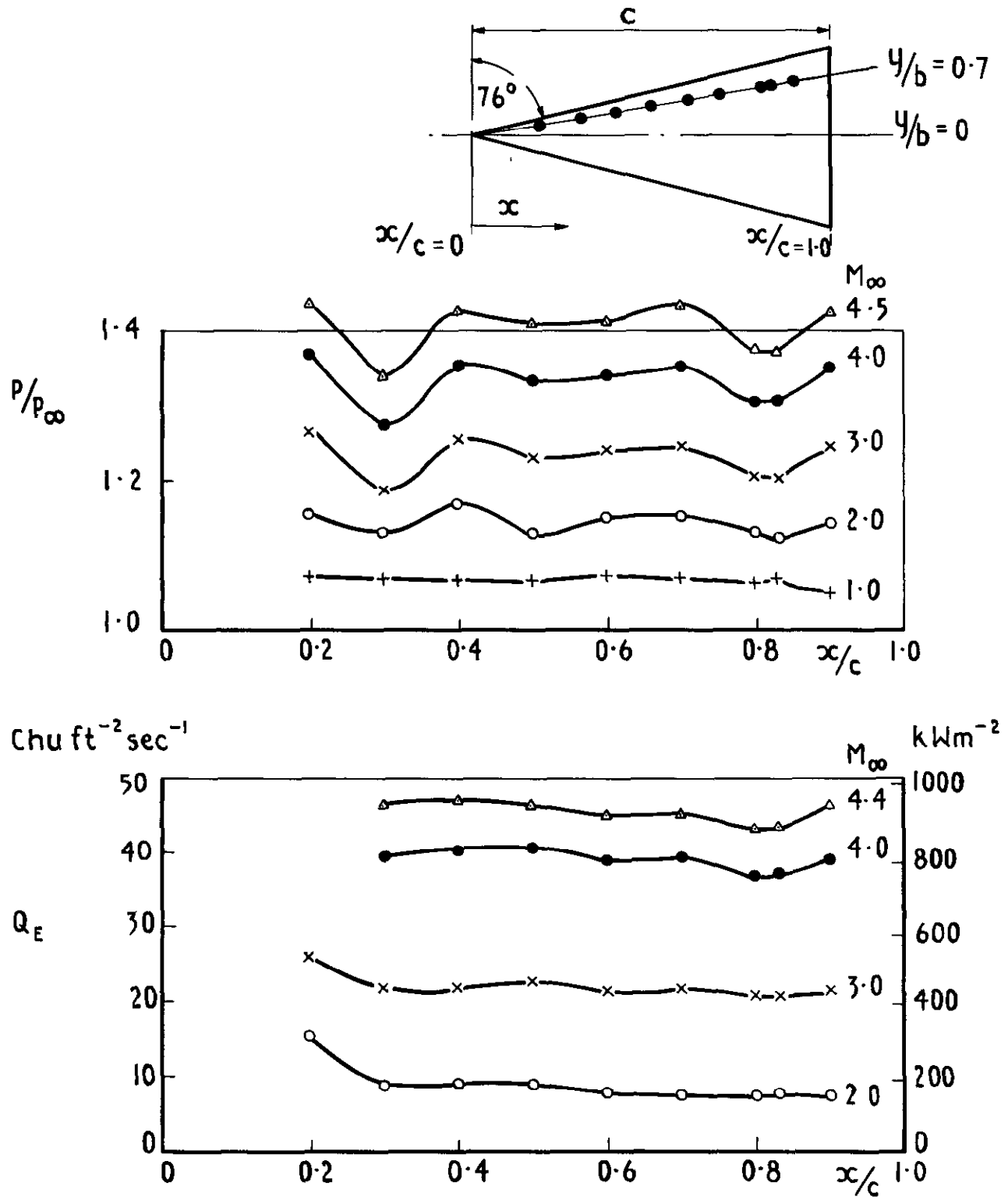

Fig 15 Distribution of pressure and heat-transfer rate along $y/b = 0{\cdot}7$ — model 2 (B L trip)

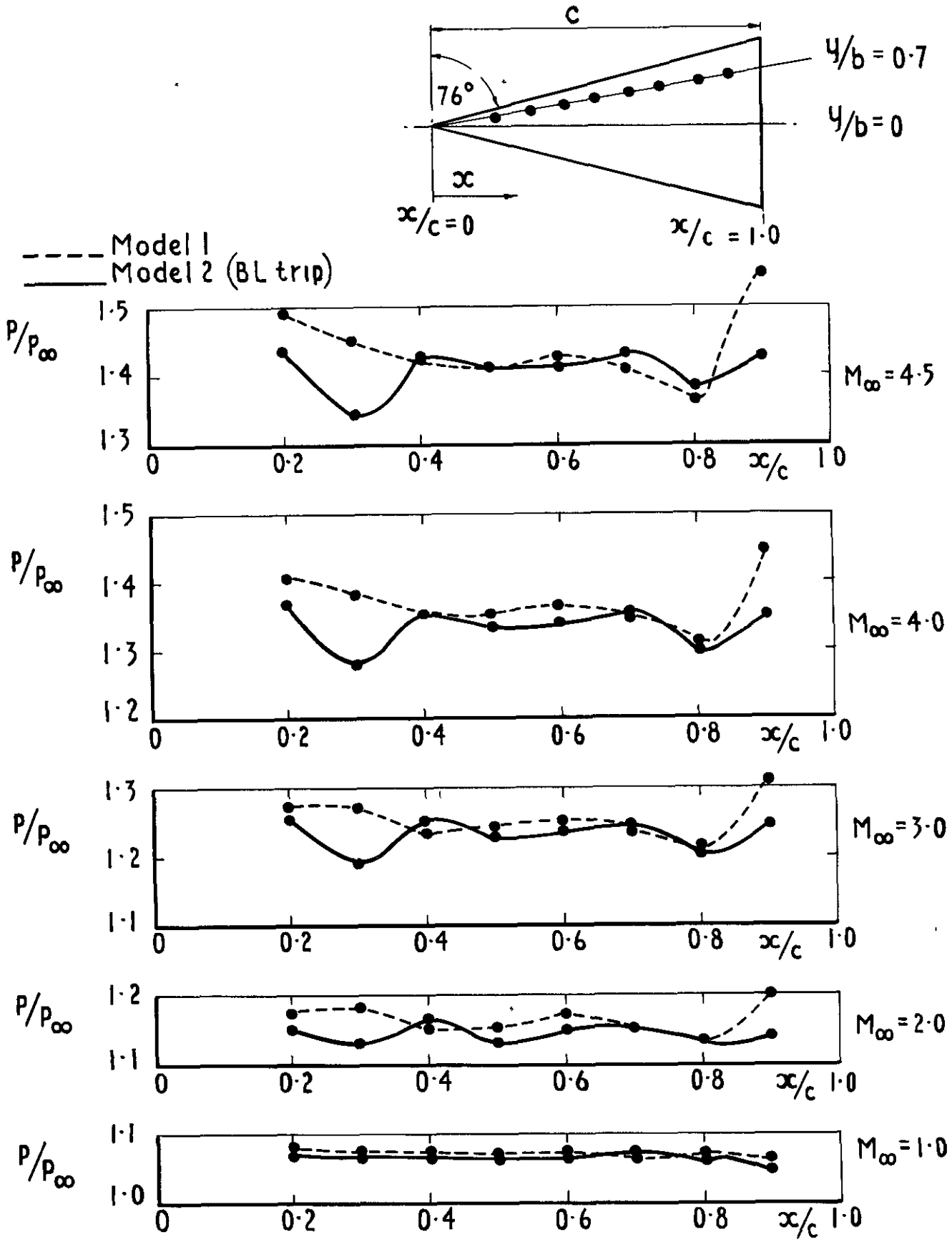

Fig 16 Comparison of pressure distribution along $y/b = 0.7$ —models 1 & 2

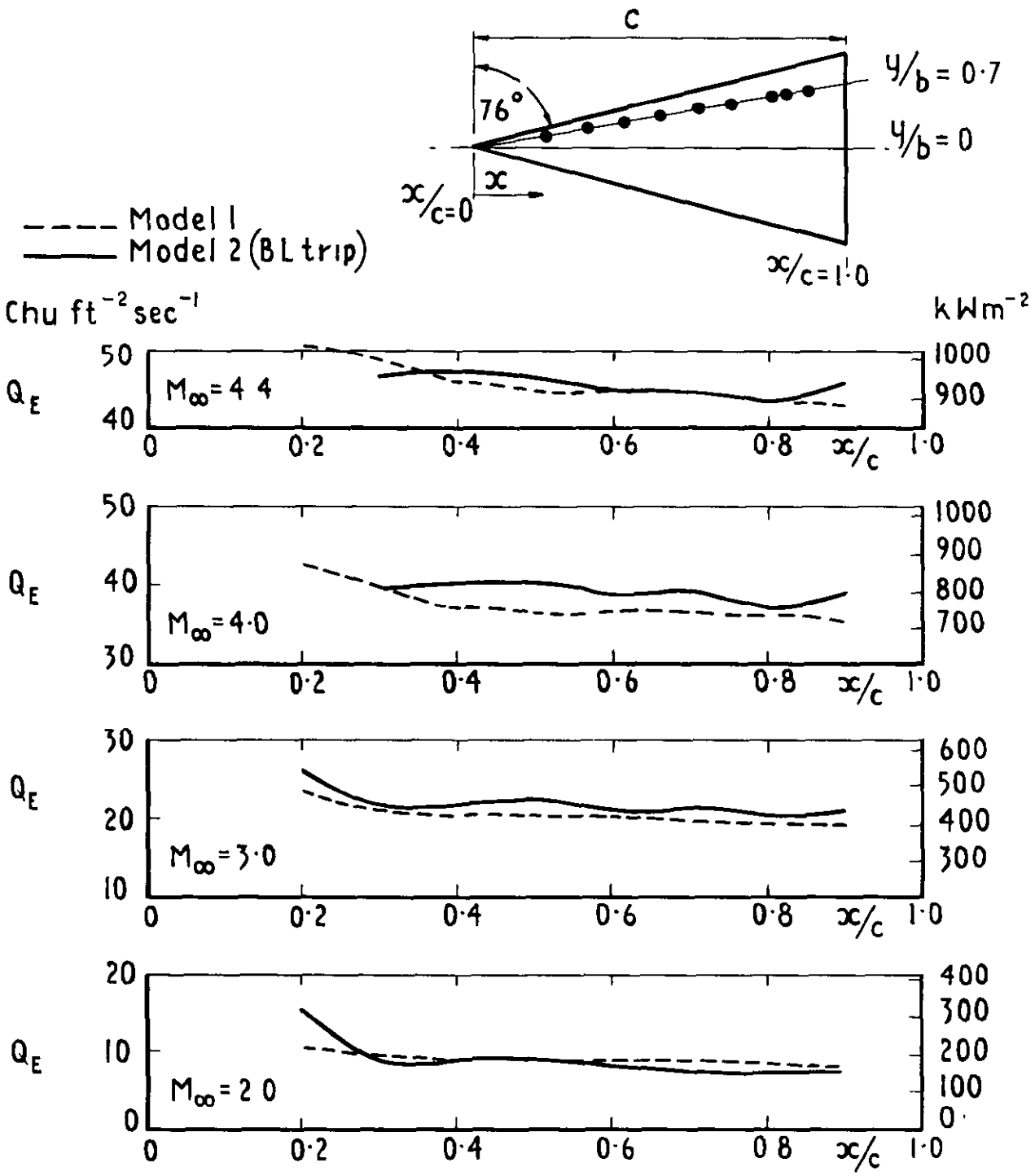

Fig 17 Comparison of heat-transfer rate along $y/b = 0{\cdot}7$ — models 1 & 2

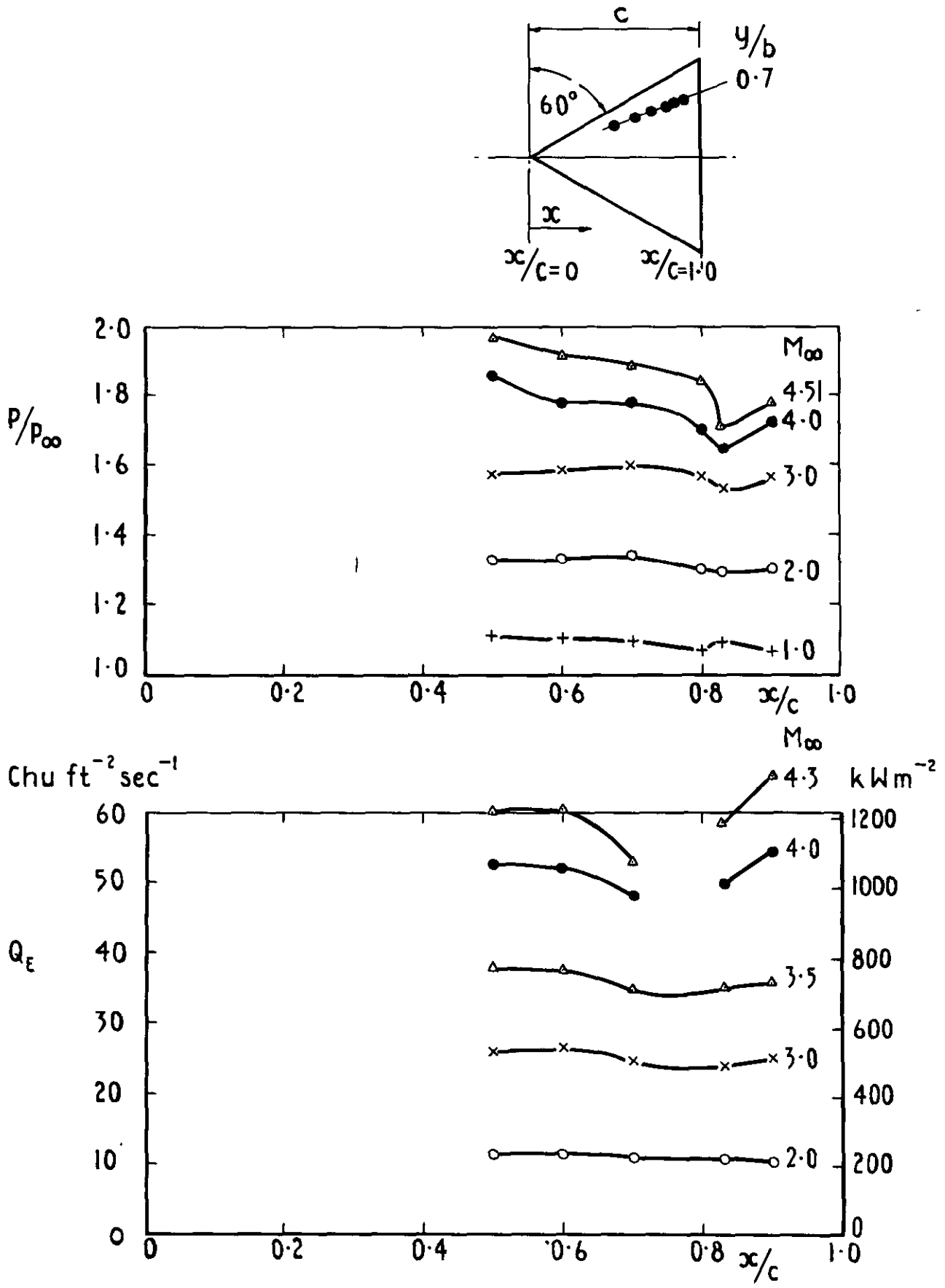

Fig 18 Distribution of pressure and heat-transfer rate along $y/b = 0{\cdot}7$ – model 3

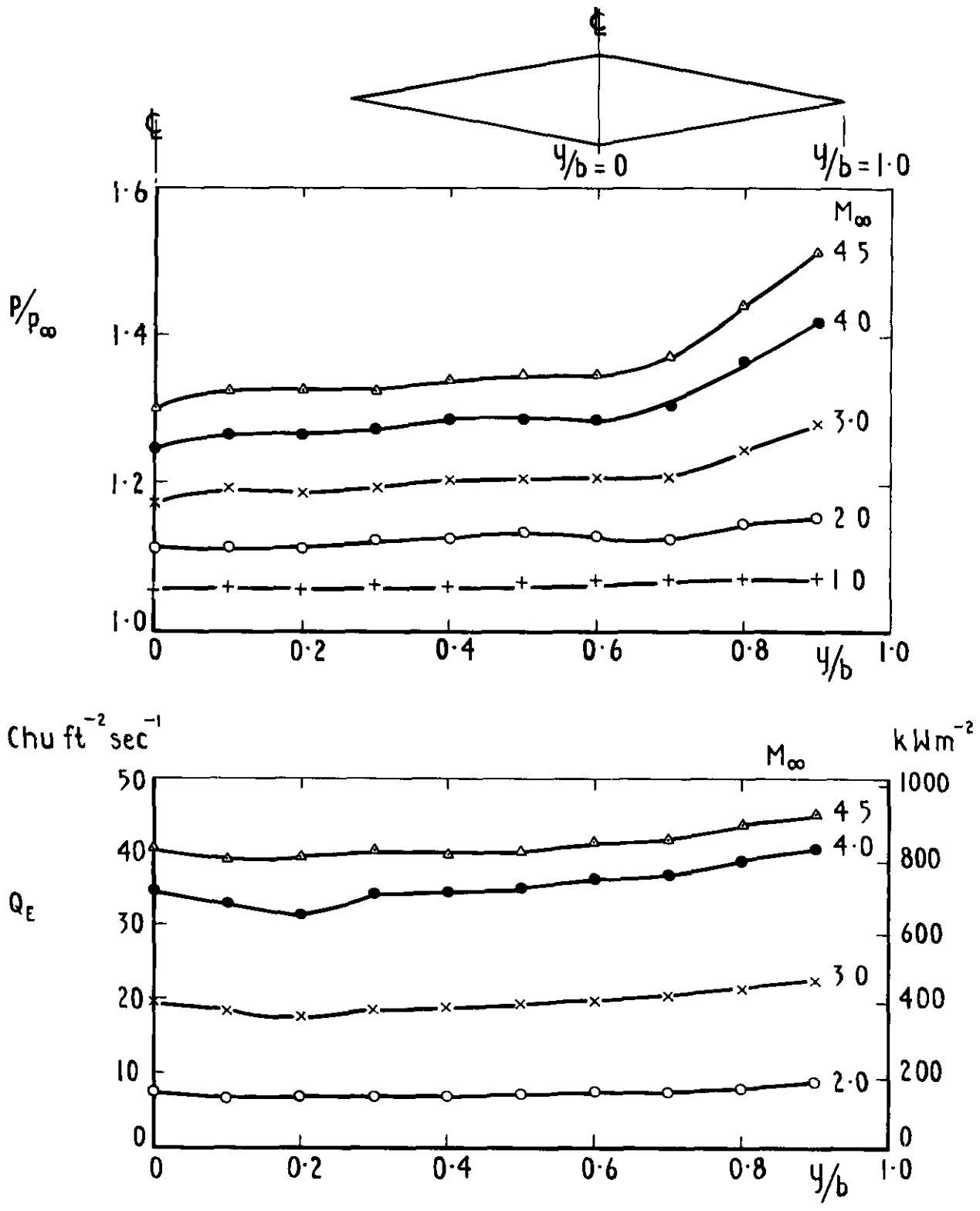

Fig 19 Spanwise distribution of pressure and heat-transfer rate (at $x/c = 0.833$) — model 2 (BL trip)

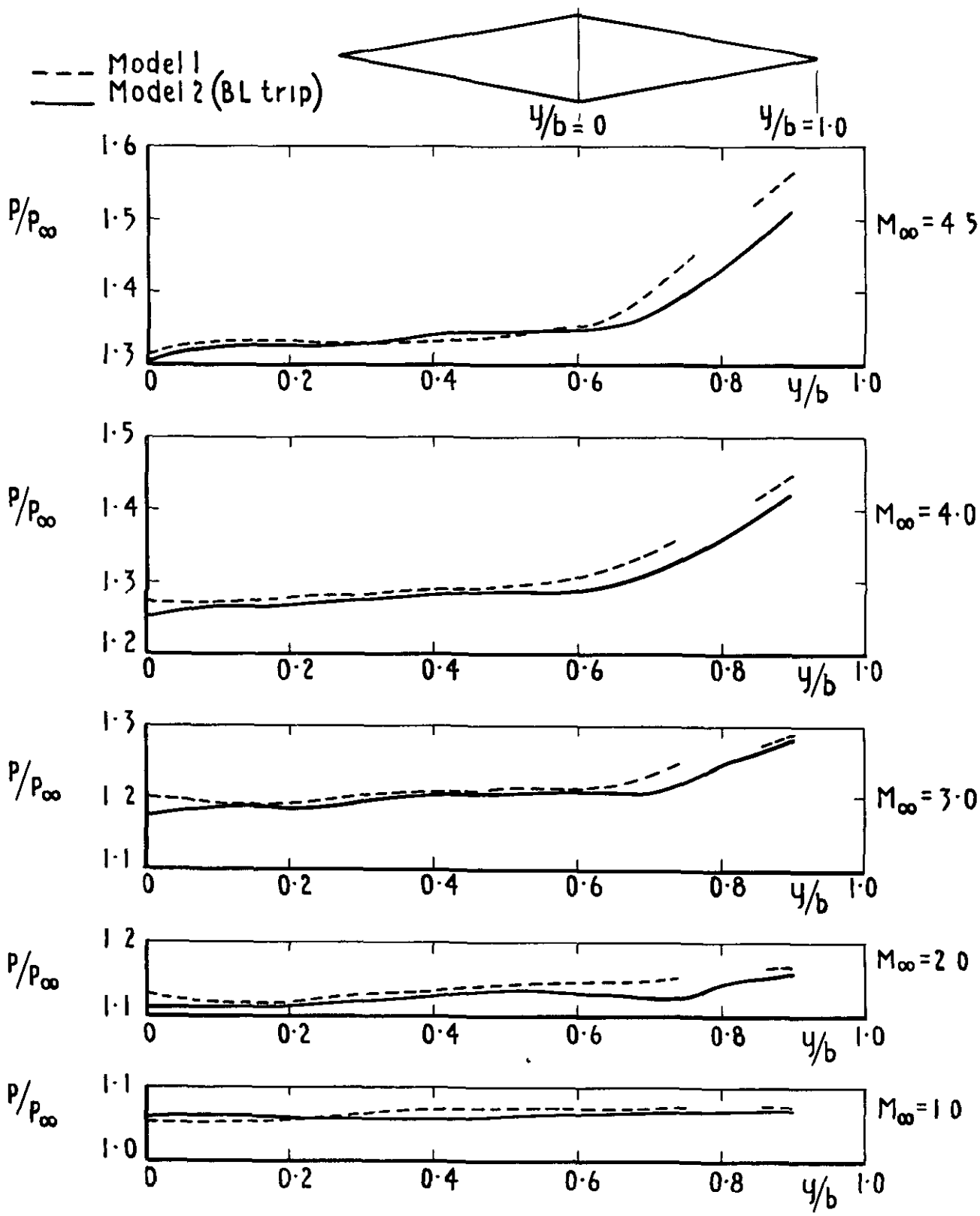

Fig 20 Comparison of spanwise pressure distribution (at $x/c = 0.833$) – models 1 & 2

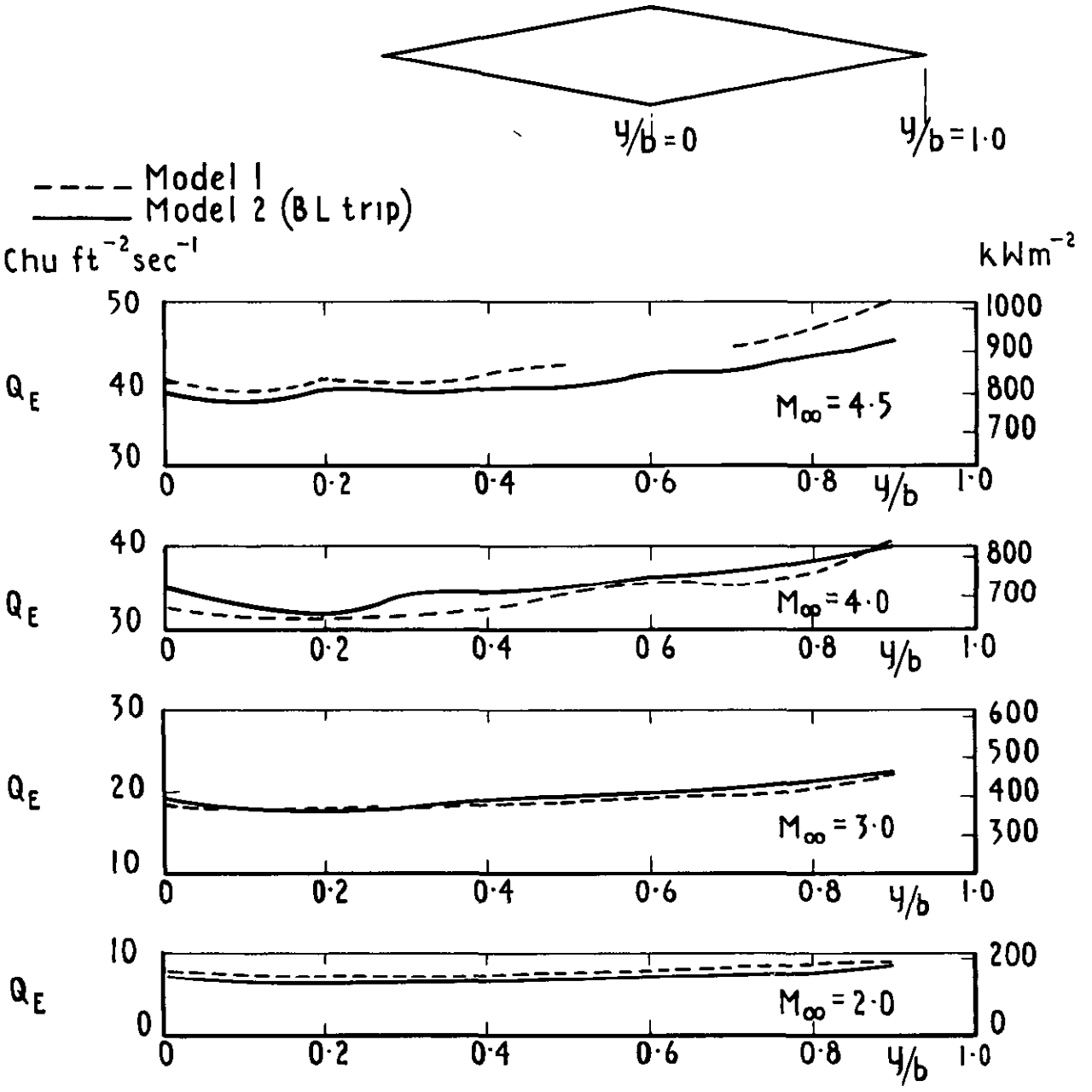

Fig 21 Comparison of spanwise heat-transfer distribution (at $x/c = 0.833$) – models 1 & 2

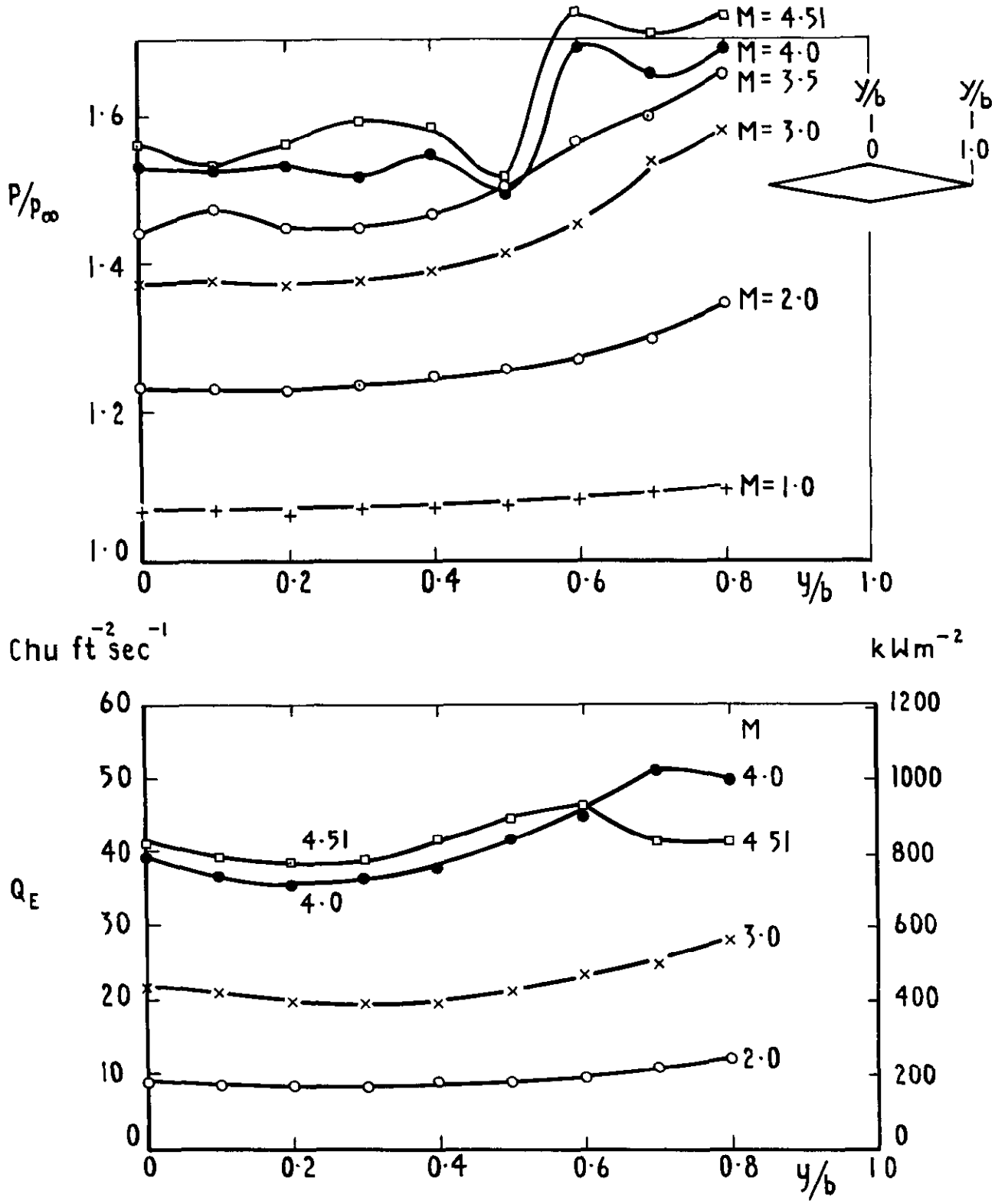

Fig 22 Spanwise distribution of pressure and heat-transfer rate (at $x/c = 0{\cdot}833$) — model 3

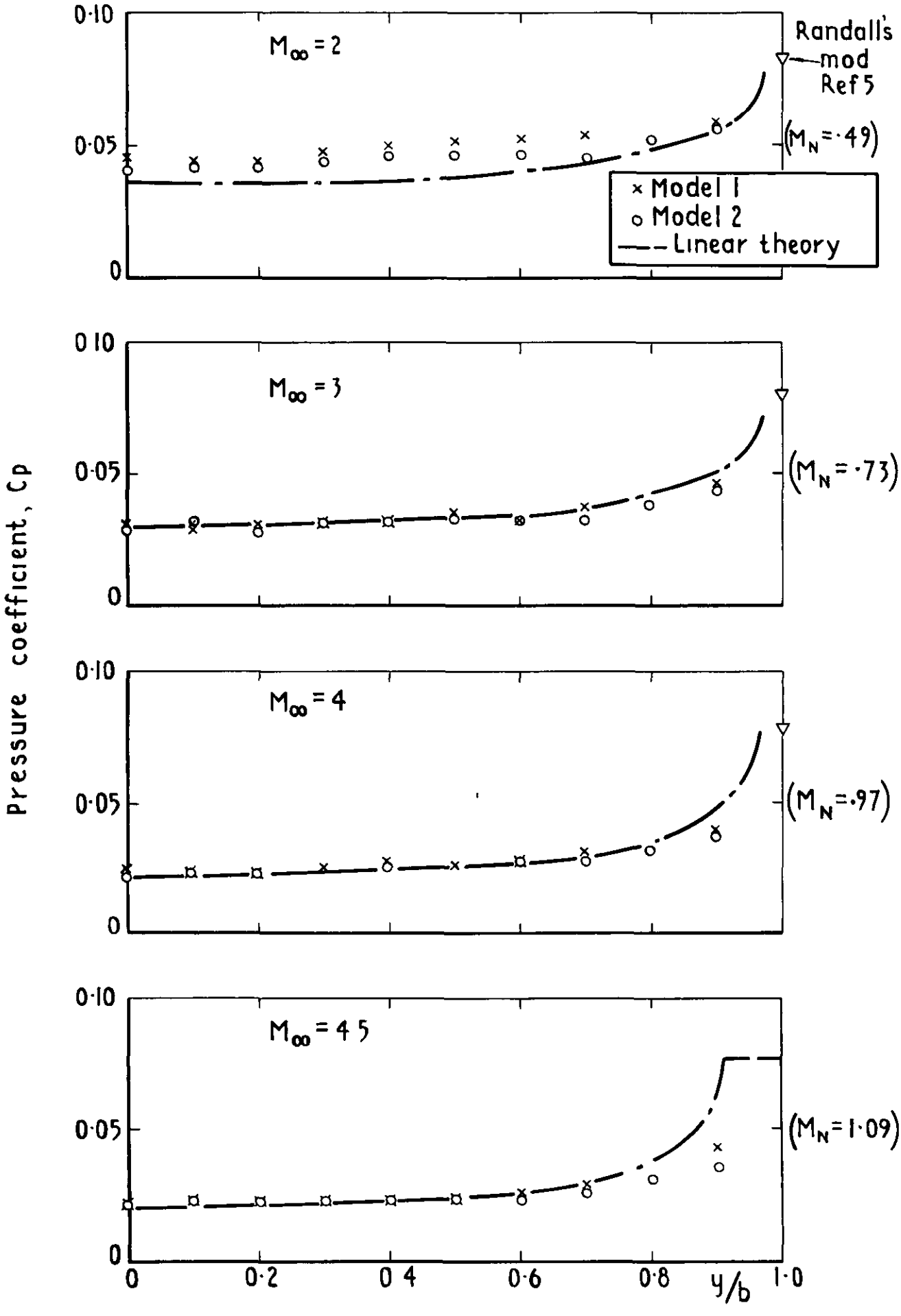

Fig 23 Comparison of measured surface pressure with linear theory – models 1 & 2

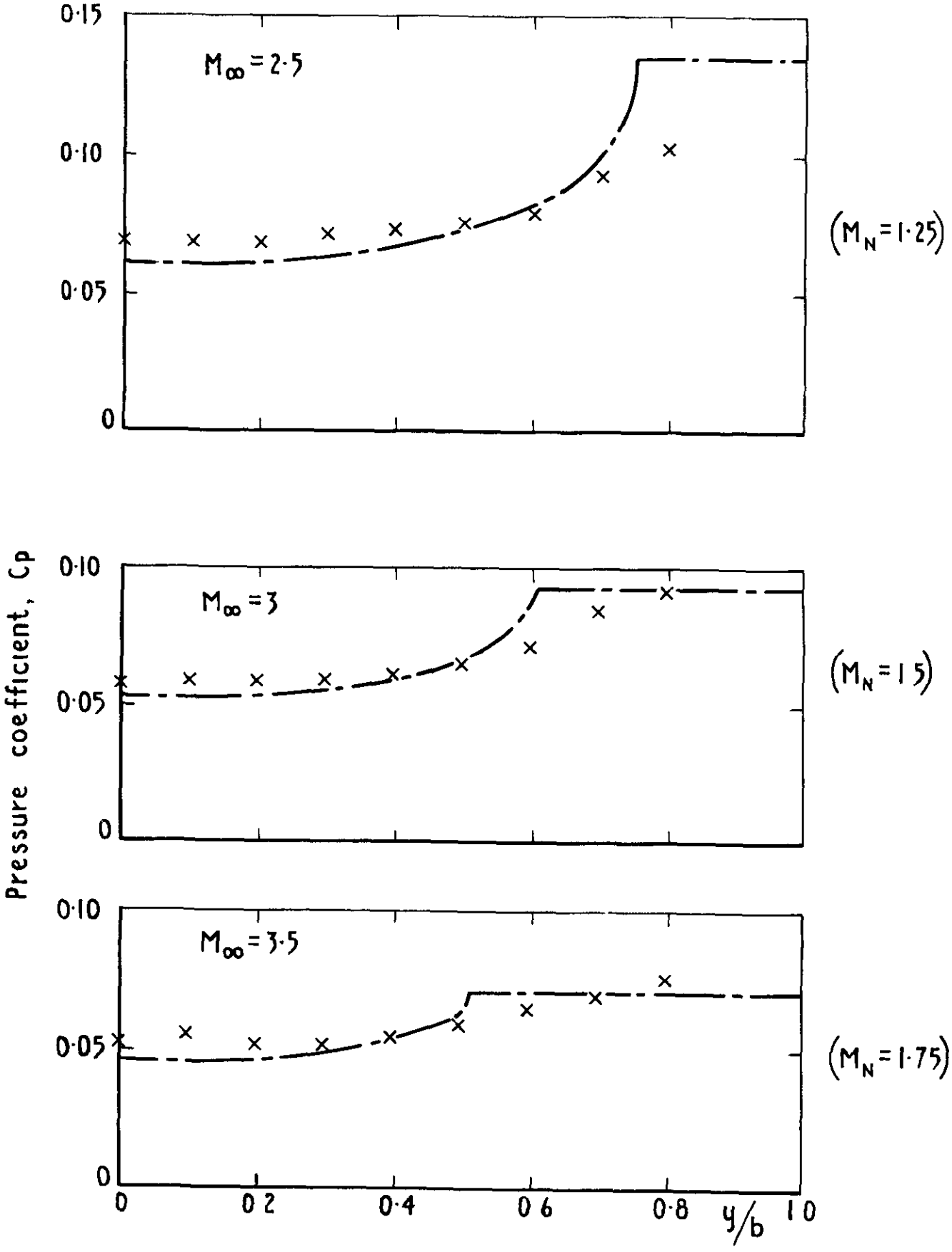

Fig. 24 Comparison of measured surface pressure with linear theory - model 3

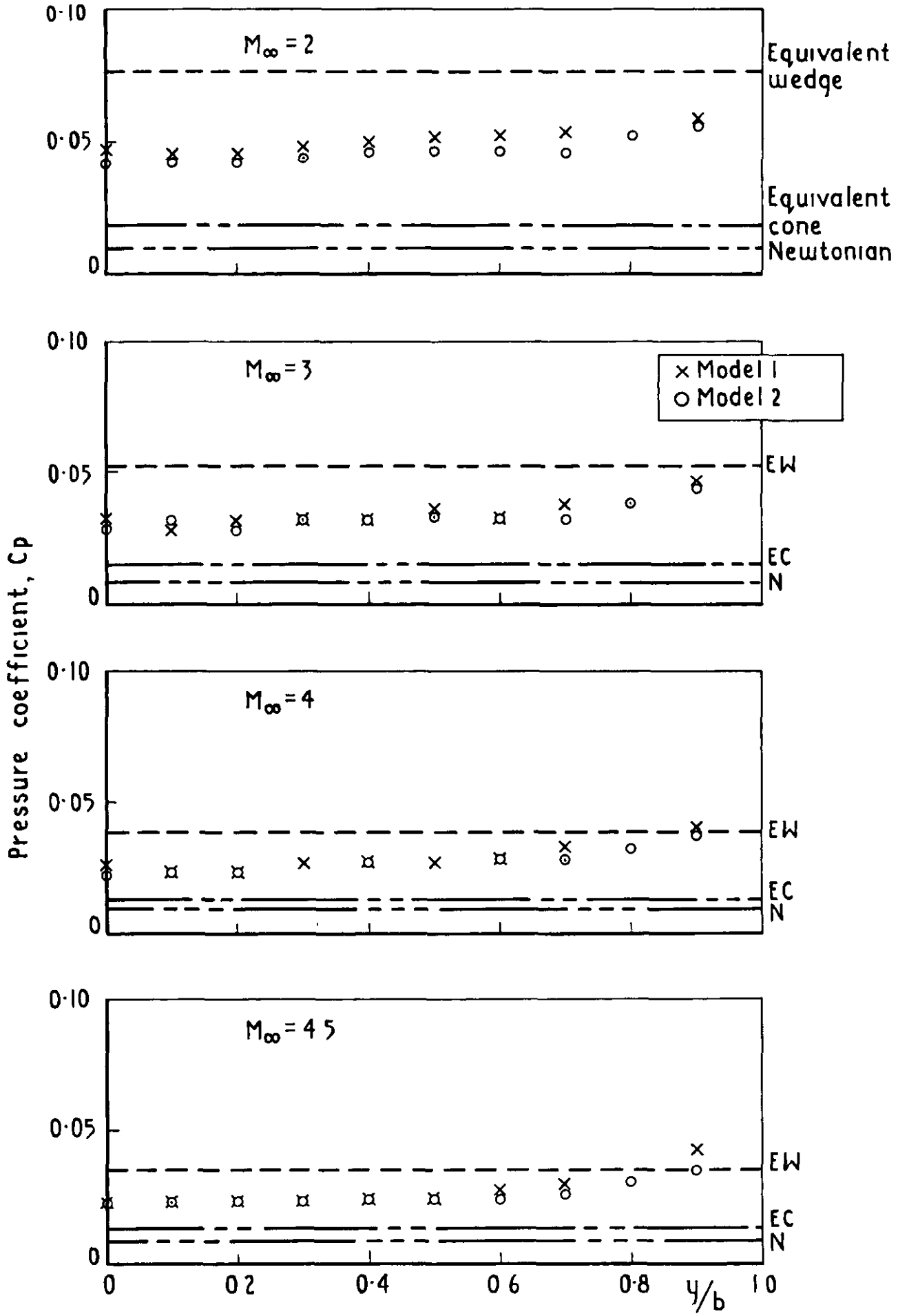

Fig 25 Comparison of measured surface pressure with approximate theories – models 1 & 2

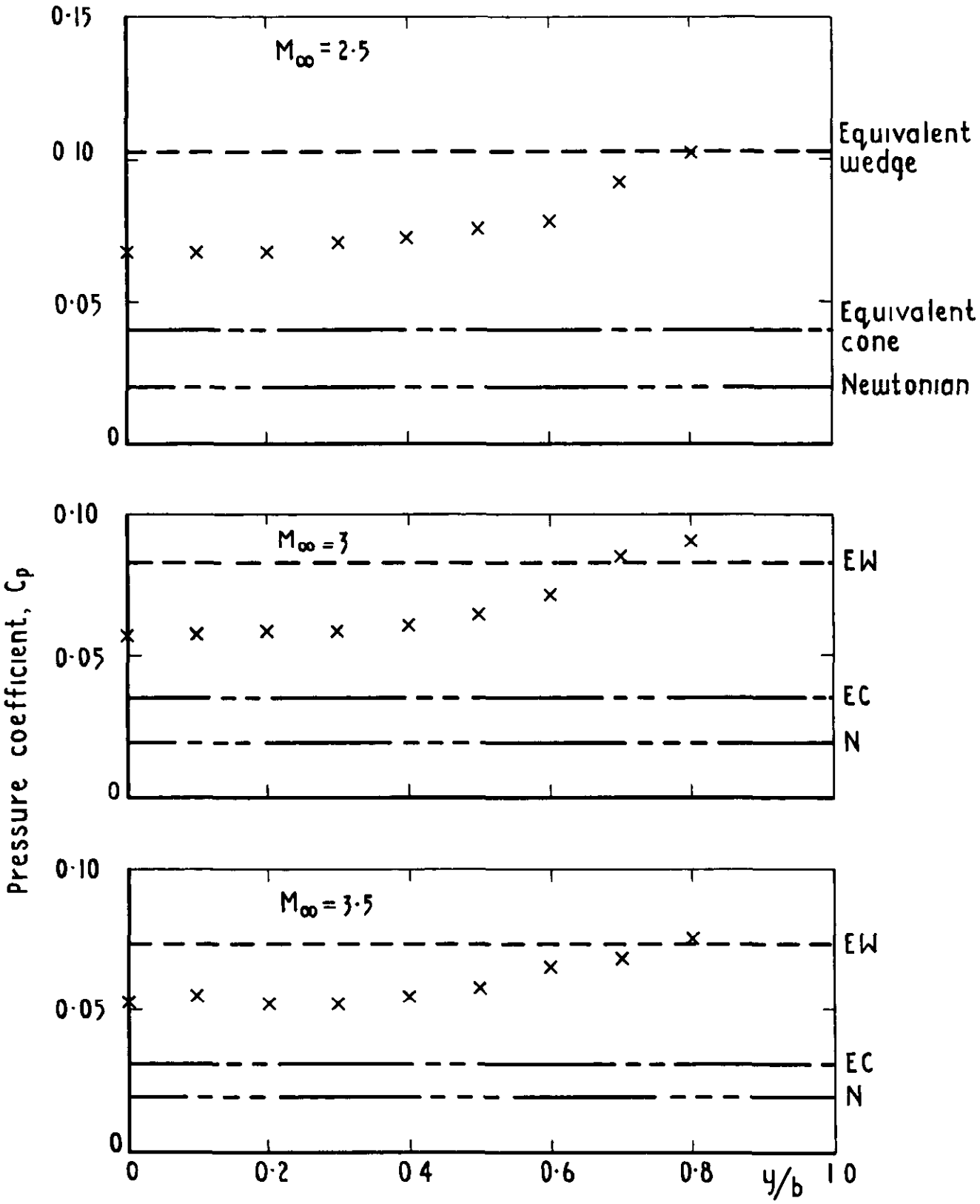

Fig 26 Comparison of measured surface pressure with approximate theories – model 3

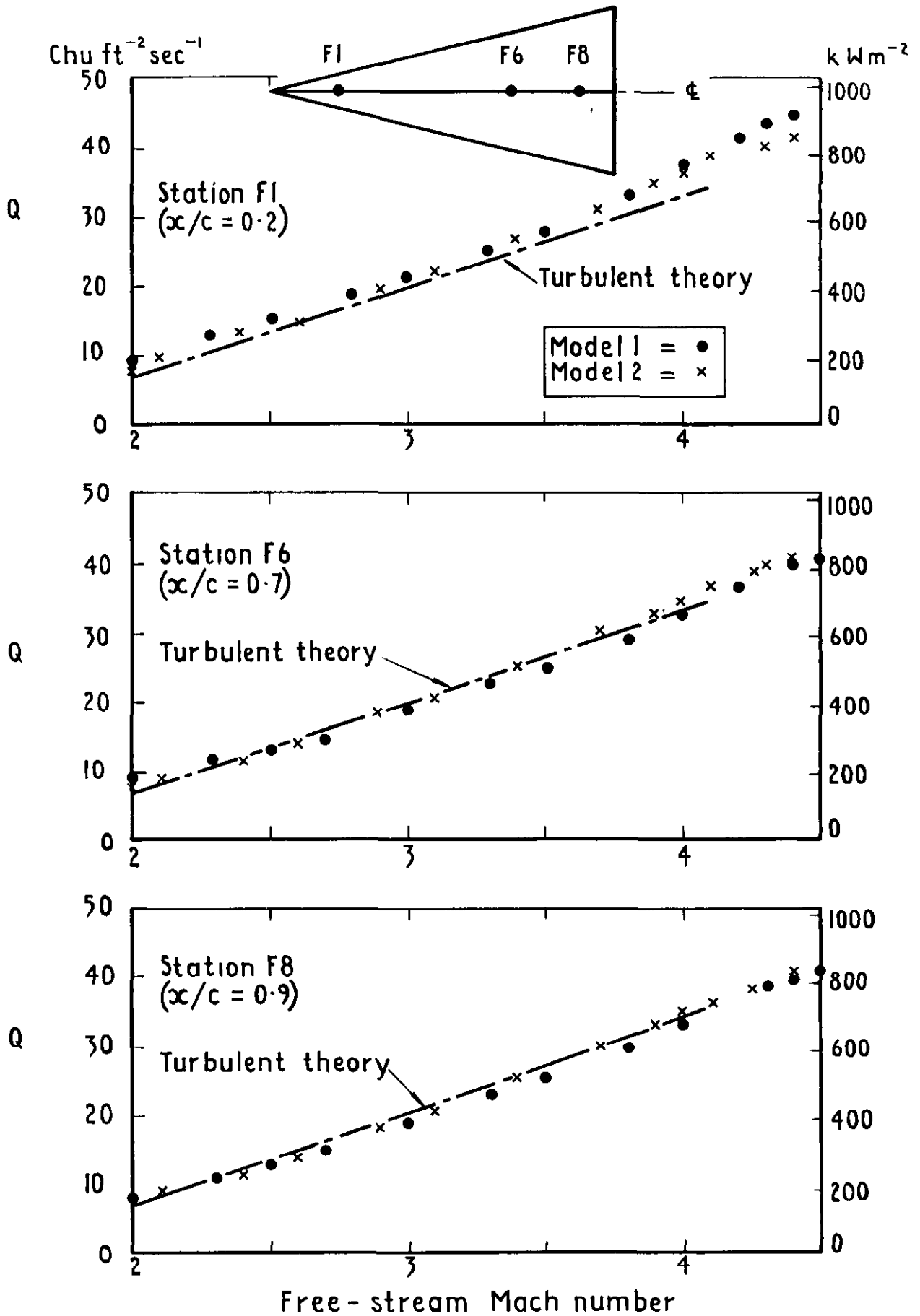

Fig. 27 Comparison of heat-transfer rate to centre-line chord with theory - models 1 & 2

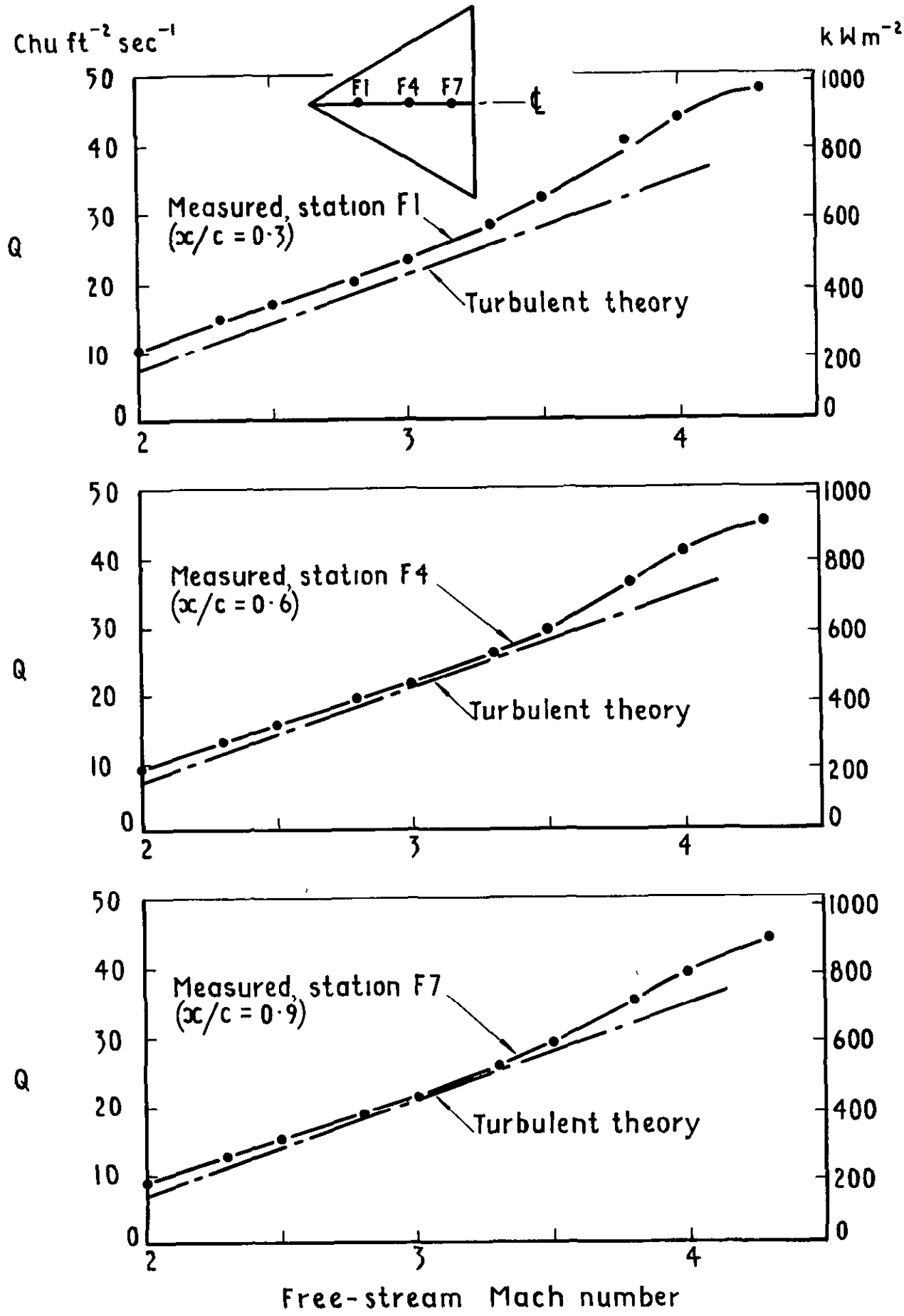

Fig 28 Comparison of heat-transfer rate to centre-line chord with theory - model 3

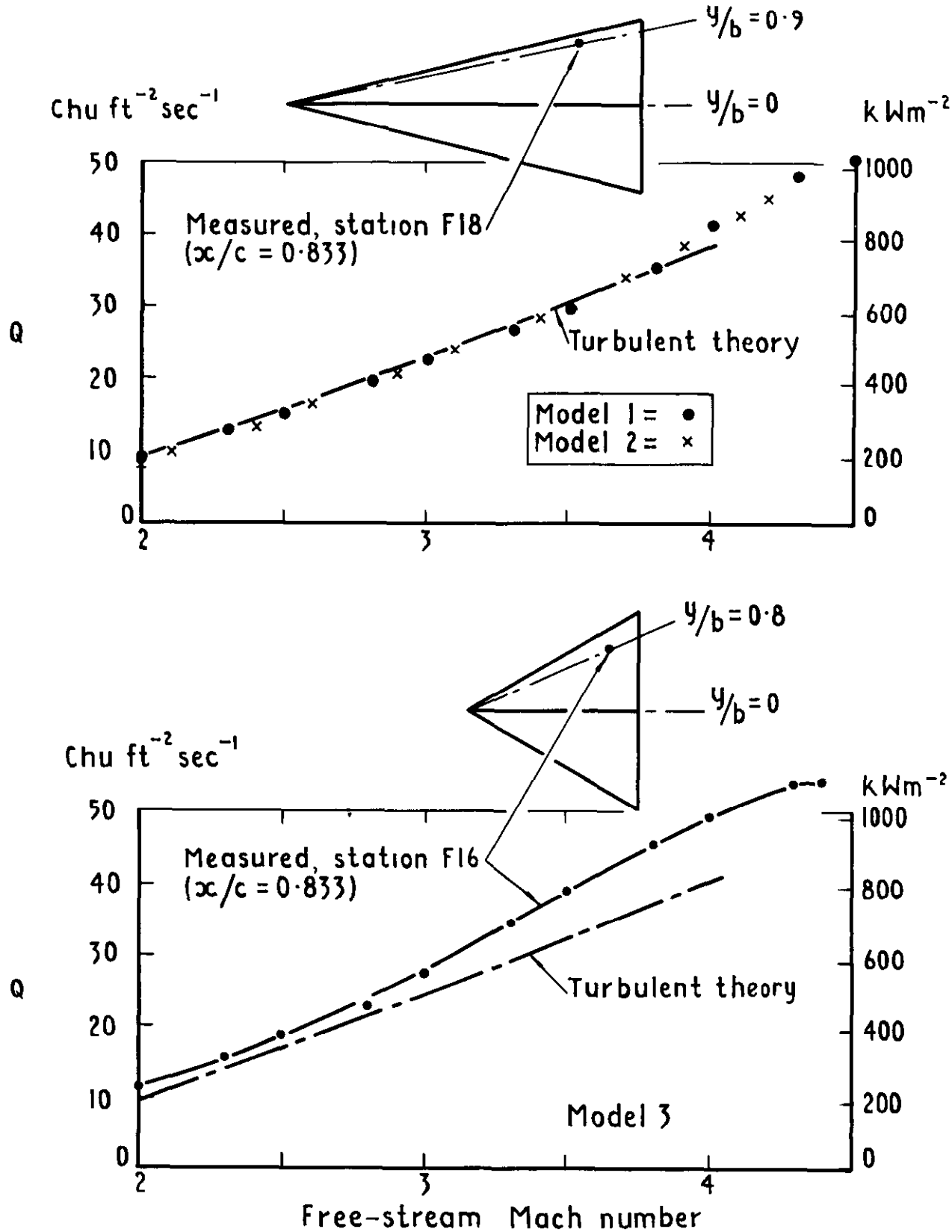

Fig. 29 Comparison of heat-transfer rate to a leading-edge station with theory - models 1, 2 & 3

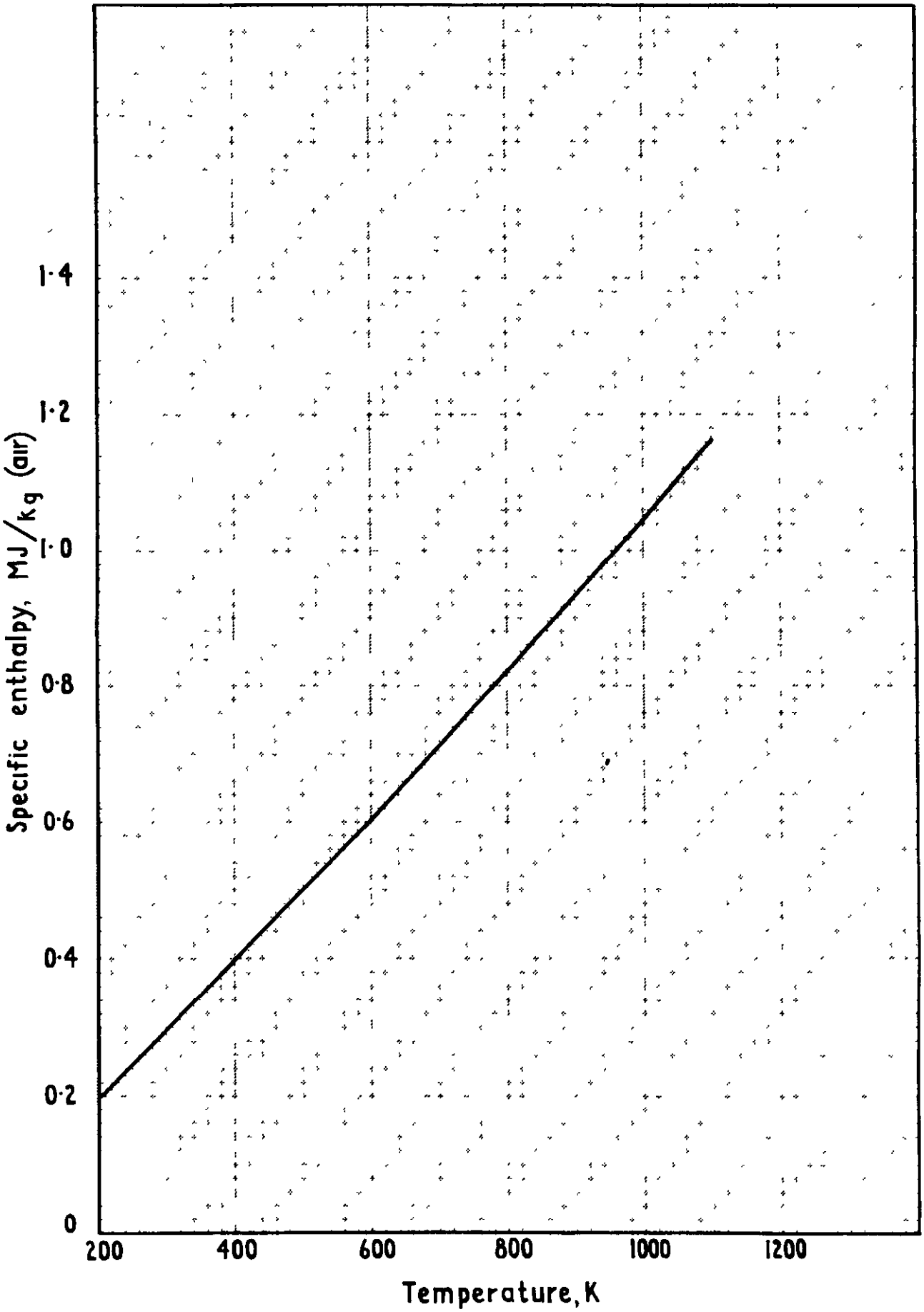

Fig. 30 Enthalpy of air v temperature

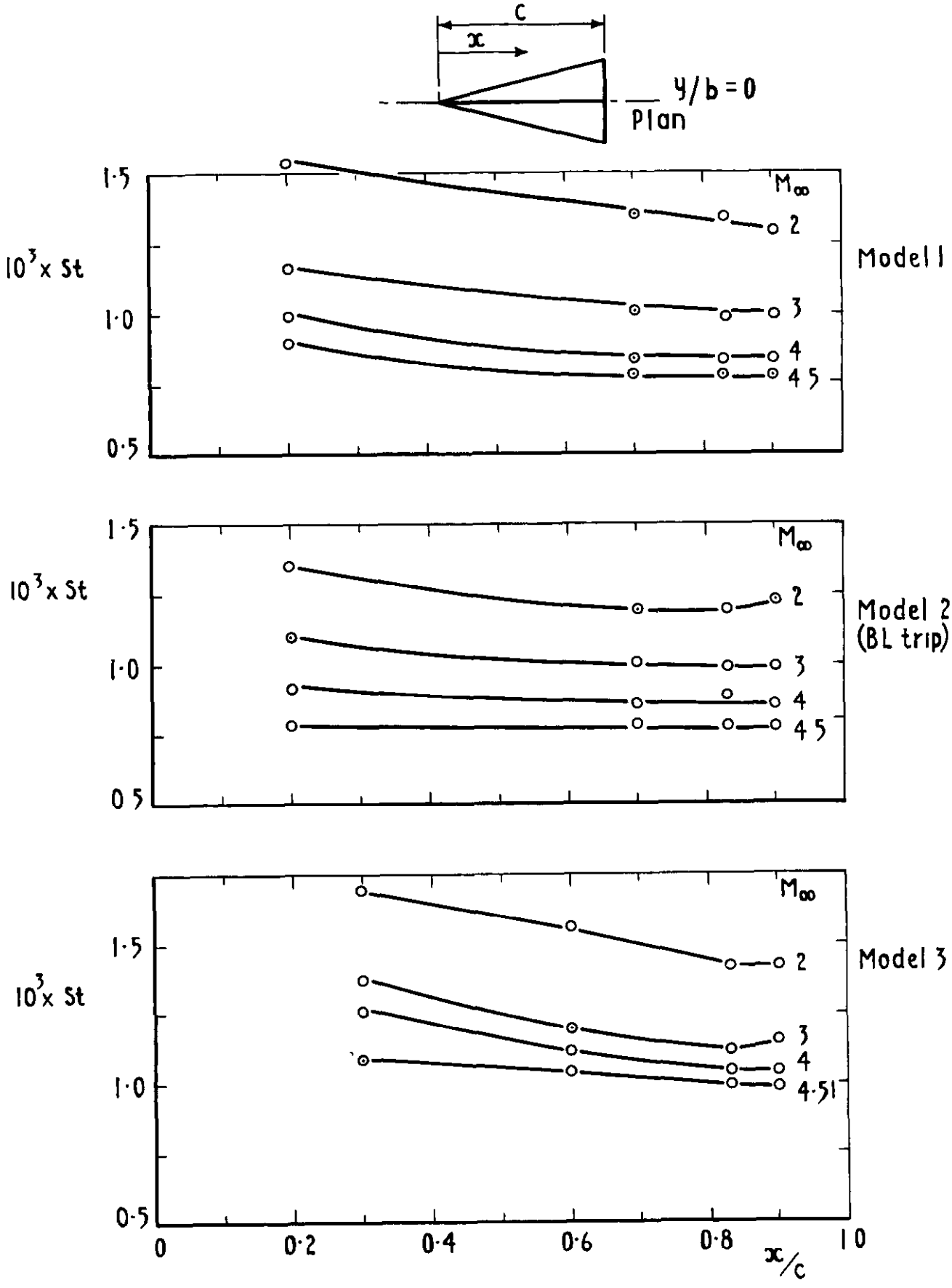

Fig 31 Variation of Stanton number along ℄ chord (Y/b=O) – all models

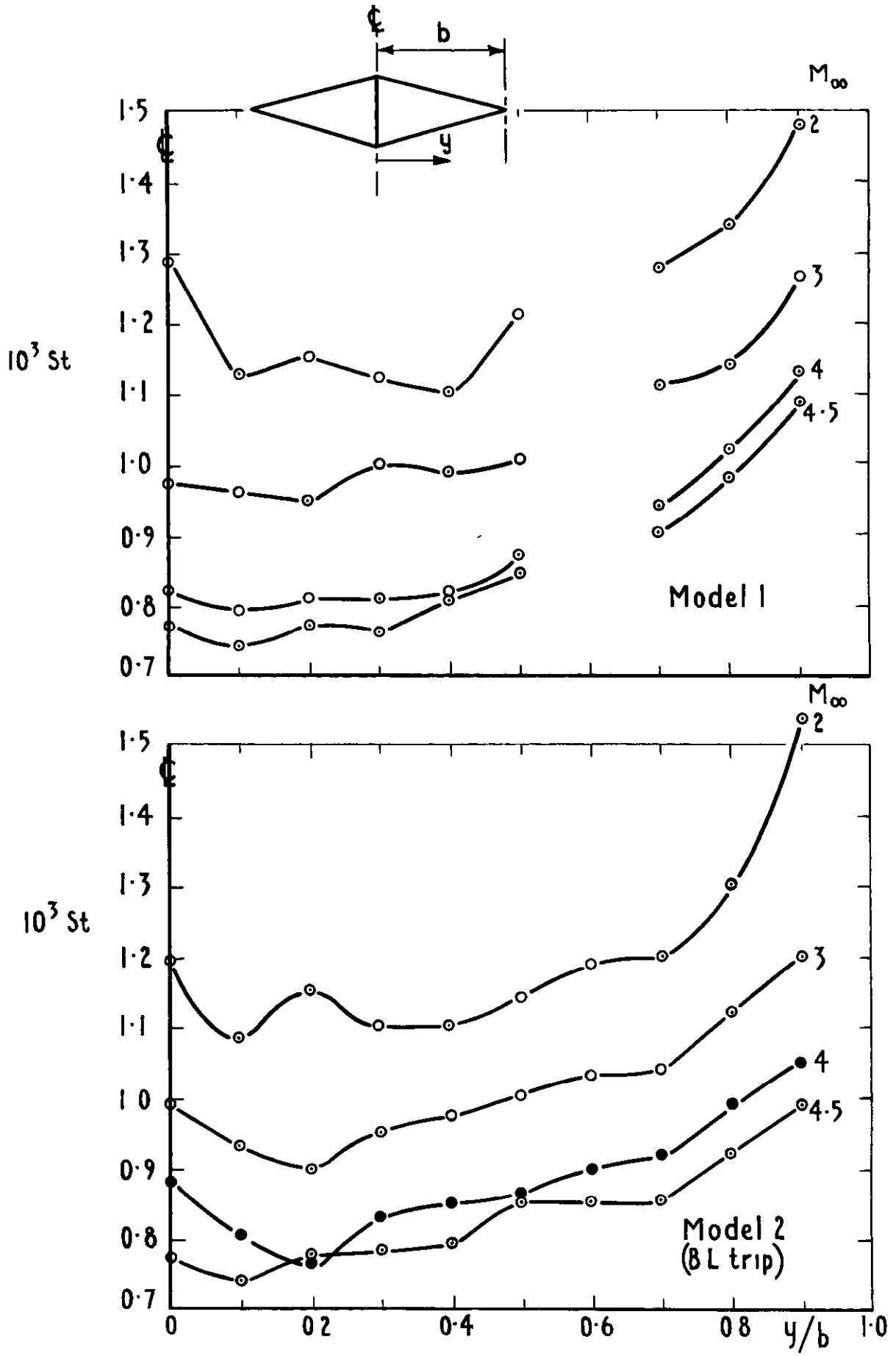

Fig. 32 Spanwise variation of Stanton number at $x/c = 0.833$ – models 1 & 2

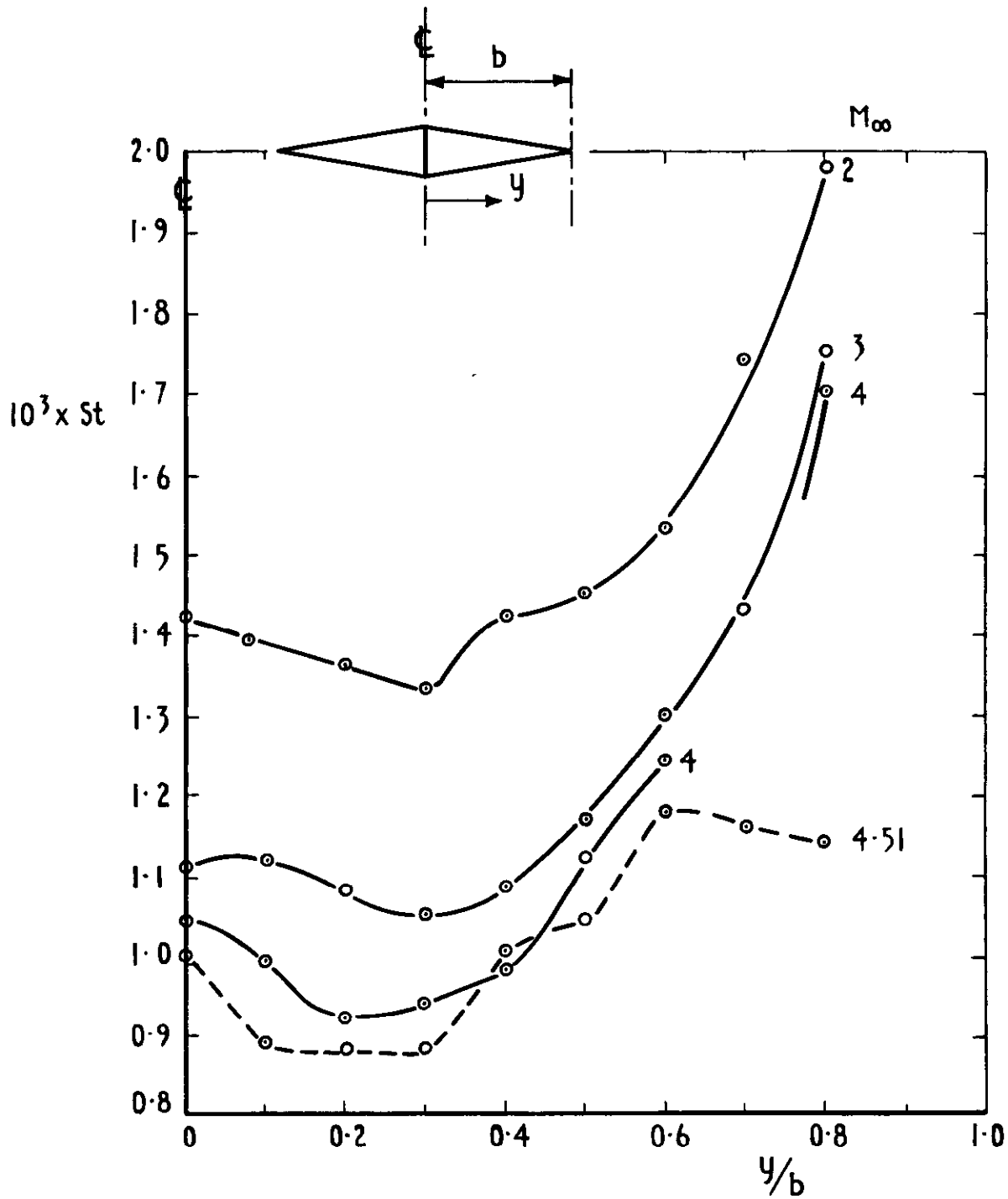

Fig. 33 Spanwise variation of Stanton number at $x/c = 0{\cdot}833$ – model 3

Printed in England for Her Majesty's Stationery Office by the Royal Aircraft Establishment, Farnborough Dd 503427 K 4

DETACHABLE ABSTRACT CARD

ARC CP No.1212
April 1971

533.693.3 ·
533.692.2
533.6 011.6 :
533.6.048.2 .
533.6.011.5

Greenwood, G. H.

HEAT TRANSFER AND SURFACE PRESSURE MEASUREMENTS ON TWO CONICAL WINGS IN FREE FLIGHT UP TO $M_\infty = 4.5$

Measurements in free flight at zero angle-of-attack have been made up to $M_\infty = 4.5$ of the heat transfer rates and surface pressures for two conical wings having sharp leading edges, diamond cross-sections and aspect ratios of 1.0 and 2.3 respectively. The heating rates are shown to be generally in good agreement with theoretical values using the 'intermediate enthalpy' method and the surface pressures are generally in good agreement with linearised theory. Part of these measurements were made in support of proposed RAE wind tunnel measurements of heat transfer.

ARC CP No.1212
April 1971

533.693.3 :
533.692.2 :
533.6.011.6 :
533.6.048.2 :
533.6.011.5

Greenwood, G. H.

HEAT TRANSFER AND SURFACE PRESSURE MEASUREMENTS ON TWO CONICAL WINGS IN FREE FLIGHT UP TO $M_\infty = 4.5$

Measurements in free flight at zero angle-of-attack have been made up to $M_\infty = 4.5$ of the heat transfer rates and surface pressures for two conical wings having sharp leading edges, diamond cross-sections and aspect ratios of 1.0 and 2.3 respectively. The heating rates are shown to be generally in good agreement with theoretical values using the 'intermediate enthalpy' method and the surface pressures are generally in good agreement with linearised theory. Part of these measurements were made in support of proposed RAE wind tunnel measurements of heat transfer.

ARC CP No 1212
April 1971

533 693 3
533.692 2
533.6 011 6
533 6 048.2
533 6 011.5

Greenwood, G H.

HEAT TRANSFER AND SURFACE PRESSURE MEASUREMENTS ON TWO CONICAL WINGS IN FREE FLIGHT UP TO $M_\infty = 4 5$

Measurements in free flight at zero angle-of-attack have been made up to $M_\infty = 4.5$ of the heat transfer rates and surface pressures for two conical wings having sharp leading edges, diamond cross-sections and aspect ratios of 1.0 and 2.3 respectively The heating rates are shown to be generally in good agreement with theoretical values using the 'intermediate enthalpy' method and the surface pressures are generally in good agreement with linearised theory. Part of these measurements were made in support of proposed RAE wind tunnel measurements of heat transfer

HER MAJESTY'S STATIONERY OFFICE

Government Bookshops

49 High Holborn, London WC1V 6HB
13a Castle Street, Edinburgh EH2 3AR
109 St Mary Street, Cardiff CF1 1JW
Brazennose Street, Manchester M60 8AS
50 Fairfax Street, Bristol BS1 3DE
258 Broad Street, Birmingham B1 2HE
80 Chichester Street, Belfast BT1 4JY

Government publications are also available through booksellers

C.P. No. 1212

SBN 11 470480 5